University of Crete

Master of Science

A Study of the Iron Line Variability in the X-Ray Spectrum of Active Galaxy MCG-6-30-15

Author:
Anastasios G. Epitropakis

Supervisor:
Prof. Iossif Papadakis

A thesis submitted in fulfillment of the requirements for the degree of M.Sc.

in the

School of Sciences and Engineering
Department of Physics

Heraklion, November 2013

"On and on
searching for a clearer view
winning and losing an inner war
wonder what we do it for
though the road seems never ending"

Brian May, *Back to the Light*

UNIVERSITY OF CRETE

Abstract

School of Sciences and Engineering
Department of Physics

M.Sc.

A Study of the Iron Line Variability in the X-Ray Spectrum of Active Galaxy MCG-6-30-15

by Anastasios G. Epitropakis

To this day, the geometry of the inner-most region of active galaxies remains unknown. A promising (and perhaps the only) way to indirectly probe this region is through X-ray variability studies. Observations reveal the presence of a strong emission line centered at 6.4 keV, interpreted as Fe Kα emission, in the X-ray spectra of active galaxies. This has led to the formulation of the so-called "illuminated disc" hypothesis, according to which the Fe line arises due to emission from a "primary" X-ray source being reflected by an accretion disc. In many cases, the profile of the Fe Kα line is found to be broad ($\sim 5-6.6$ keV) and "skewed" towards longer wavelengths, which is indicative of material orbiting close to a black hole.

The above observational facts stimulated an ongoing attempt to identify and study correlations, in the form of temporal delays, between light-curves that are thought to represent "reflected" (traditionally identified with the $0.5-1.5$ keV band) and "primary" (traditionally identified with the $2-4$ keV band) emission components envisaged in an "illuminated disc" scenario. Studies of such delays have so far indicated that the data are consistent with an "illuminated disc" scenario in its simplest form.

In this work I focused my attention on a particular active galaxy, MCG$-$6-30-15, since (a) it was the first one for which a broad Fe Kα line was observed, (b) it is a bright source of X-rays, and (c) it has been observed by many satellites. I collected all available data from both the *Suzaku* and *XMM-Newton* X-ray satellites. This is the first time that data from the former satellite has been used to estimate delays. The purpose of my work is, first of all, to use data from both satellites in order to constrain the delays between the "reflected" and "primary" emission that have already been observed in MCG$-$6-30-15, and secondly to estimate, for the first time, the delays between the Fe Kα line itself (which is expected to be a clearer signature of reflection than the traditionally used $0.5-1.5$ keV band) and the "primary" emission. My results indicate that the delays between the line and the "primary" X-ray source are not consistent with a simple "reflection scenario", while it remains unclear whether *Suzaku* and *XMM-Newton* data can be reliably combined in order to constrain the delays.

Acknowledgements

Firstly, I would like to express my sincerest gratitude to my supervisor, Prof. Iossif Papadakis, for his continued guidance, motivation, patience, and faith in my abilities. I can only hope that our collaboration will continue to be as stimulating, fruitful and resourceful to me as it has been for the past two years. Secondly, to my dear partner, for her continuous support, patience and understanding during the times I had to focus all of my attention on writing this thesis and/or refining my understanding of the subject, and my brother, for always managing to brighten my mood, even during the hardest of times. And last, but not least, I wish to reserve a special place in order to thank my parents and the rest of my family, both in Greece as well as in the Netherlands, for their support (the financial −apart from the ever-present moral− component of which is wholeheartedly appreciated!).

This thesis was completed as part of the graduate programme co-financed by the Act "Scholarships programme SSF (State Scholarships Foundation/IKY) with an individualized assessment process of the Academic Year 2012-2013" from resources of the Operational Programme "Education and Lifelong Learning", of the European Social Fund (ESF), the NSRF 2007-2013.

Contents

List of Figures

List of Tables

Abbreviations

ACF	:	Auto-covariance function
AGN	:	Active galactic nucleus
ApJ	:	The Astrophysical Journal
BH	:	Black hole
CCF	:	Cross-covariance function
CS	:	Cross-spectrum
DFT	:	Discrete Fourier transform
DOF	:	Degrees of freedom
ESA	:	European Space Agency
EW	:	Equivalent width
GR	:	General relativity/general-relativistic
IC	:	Inverse-Compton
MNRAS	:	Monthly Notices of the Royal Astronomical Society
PASJ	:	Publications of the Astronomical Society of Japan
PSD	:	Power spectral density
SAA	:	South Atlantic Anomaly
SED	:	Spectral energy distribution
SMBH	:	Super-massive black hole
UV	:	Ultra-violet

Physical and Astronomical Constants

Speed of light in vacuo	c	=	$2.99792458 \times 10^{10}$ cm s^{-1} (exact)
Gravitational constant	G	=	$6.67259(85) \times 10^{-8}$ cm^3 g^{-1} s^{-2}
Elementary charge	e	=	$4.8032068(14) \times 10^{-10}$ esu
Electron mass	$m_{\rm e}$	=	$9.1093897(54) \times 10^{-28}$ g
Proton mass	$m_{\rm p}$	=	$1.6749286(10) \times 10^{-24}$ g
Boltzmann constant	$k_{\rm B}$	=	$1.380658(12) \times 10^{-16}$ erg K^{-1}
Electron-volt	eV	=	$1.6021772(50) \times 10^{-12}$ erg
Astronomical unit	AU	=	1.496×10^{13} cm
Parsec	pc	=	3.086×10^{18} cm
Light-year	ly	=	9.463×10^{17} cm
Solar mass	$\rm M_\odot$	=	1.99×10^{33} g
Solar radius	$\rm R_\odot$	=	6.96×10^{10} cm
Solar luminosity	$\rm L_\odot$	=	3.9×10^{33} erg s^{-1}

Symbols

M	mass
t	time
L	luminosity
ω	angular frequency
ν	frequency
f	fraction
Γ	photon index
E	energy, expectation operator
EW	equivalent width
FE	fractional exposure
T	temperature/time
$\Psi(t)$	response function
$\tilde{\Psi}(\omega)$	transfer function
r	radius/radial coordinate/positive integer
F	flux
R_{g}	gravitational radius
ξ	ionisation parameter
A	elemental abundance (w.r.t. solar)
q	power-law index
i	inclination angle
i	imaginary unit
π	circle circumference/diameter
H_0	Hubble constant
z	redshift
Ω_{M}	matter (baryonic+dark) density (w.r.t. critical)

Ω_Λ	dark energy density (w.r.t. critical)
$X(t)$	light-curve/stationary random process
τ	time-lag
Δt	temporal width
h	height
μ	mean value
σ^2	variance
σ	standard deviation
d	degrees of freedom
a	constant
b	constant
$R(\tau)$	auto-covariance function
$G(\omega)$	Fourier coefficient of $X(t)$
$h(\omega)$	power spectral density
N	positive integer
n	particle number density/positive integer
m	positive integer
χ^2	chi-square
$P_{\rm null}$	probability for accepting the null hypothesis
$\zeta_X(\omega)$	discrete Fourier transform of $X(t)$
$h_{12}(\omega)$	cross-spectrum between $X_1(t)$ and $X_2(t)$
$R_{12}(\omega)$	cross-covariance function between $X_1(t)$ and $X_2(t)$
$\phi_{12}(\omega)$	phase spectrum between $X_1(t)$ and $X_2(t)$
$\tau_{12}(\omega)$	time-lag spectrum between $X_1(t)$ and $X_2(t)$
$\gamma_{12}(\omega)$	coherence function between $X_1(t)$ and $X_2(t)$

To my father, for supporting me in his own way.

Chapter 1

Introduction

1.1 Active Galactic Nuclei

The term *active galactic nuclei* (AGN) refers to the compact regions at the centres of galaxies where phenomena of non-stellar origin are observed. There exist several types of AGN according to their observational properties, such as quasars, blazars, radio galaxies and Seyferts. Approximately 43% of nearby galaxies can be regarded as "active", while Seyfert galaxies comprise a corresponding fraction $\sim 10\%$ (Ho, Filippenko & Sargent 1997). AGN are also broadly classified as either "Type 1" or "Type 2", depending on whether or not broad optical emission lines are observed in their spectra. The main defining characteristics that set AGN apart from "regular" galaxies are their large luminosities ($\sim 10^9 - 10^{15}$ $L_\odot$) originating from small regions ($\lesssim 10$ AU), non-thermal continuum spectra spanning many orders of magnitude in frequency (typically from radio all the way to X- and γ-rays), highly collimated jets observed in $\sim 10\%$ of them, broad and narrow emission lines and prominent variability at all wavelengths.

The origin of these peculiar characteristics are not fully understood yet. According to the currently accepted paradigm, the large inferred luminosities originating in the compact centers of galaxies that host an AGN are the result of gravitational energy being converted into radiation by accretion of material onto a supermassive ($\gtrsim 10^6$ $M_\odot$) compact object (presumably a black hole; BH), a hypothesis first introduced by Salpeter and Zel'dovich in 1964 and Lynden-Bell in 1969. In particular, it is now thought that the engine that powers AGN is material, in the form of an accretion disc, being forced to spiral through dissipative processes into the gravitational well of the compact object, heating up and radiating in the process (Shakura & Sunyaev 1973).

According to current unification schemes the broad emission lines seen in the optical spectra of "Type 1" AGN are observed due to small inclination angles (typically $\lesssim 40°$). In particular, it is thought that the central engines in "Type 1" AGN are directly viewed with minimal obscuration, revealing the presence of a multitude of gas clouds that orbit close to the central BH and are being irradiated by photons emitted

by the accretion disc, therefore giving rise to the observed broad optical emission lines. On the other hand, "Type 2" AGN are thought to be observed at high inclination angles (typically $\sim 40^\circ - 90^\circ$) which causes the central engine to be obscured by large amounts of material, perhaps in the form of a dusty torus, hence the observed optical emission lines originate mostly from gas that is being irradiated far from the central engine where orbital velocities are low (Antonucci 1993).[1]

Apart from its simplicity, the BH paradigm offers a variety of arguments in its favour instead of more complicated models based on regular stellar processes that have been proposed in the past. Examples of such models include supernovae chain explosions, high star formation rates and pulsar clusters (e.g. Burbidge 1961; Cameron 1962; Spitzer & Saslaw 1966; Arons, Kulsrud & Ostriker 1975). The main arguments in favour of the BH paradigm can be summarised as follows:

- The release of gravitational energy by means of accretion can potentially yield up to ~ 10 times greater efficiencies[2] than thermonuclear fusion that powers stars. This can explain the large inferred AGN luminosities.
- The very nature of a BH provides a natural explanation of the compactness of, in particular, the X-ray emitting region in AGN, as inferred from the rapid variability (~ 1 h) typically observed in their light-curves at said wavelengths.
- Standard accretion disc theory (the so-called α-disc model; Shakura & Sunyaev 1973) predicts a characteristic peak in the spectrum of the radiating gas at ultraviolet (UV) wavelengths, which is thought to be related to an observed UV feature in AGN spectral energy distributions (SEDs) that is commonly referred to as the "big blue bump".

The necessity of assuming that accretion takes place on a super-massive object can be inferred from the following argument: Assuming spherical accretion of purely ionised H onto a BH of mass M, then an observed bolometric (i.e. total) luminosity of $\sim 10^{12}$ $\mathrm{L}_\odot$ for an AGN radiating at its Eddington limit ($\sim 10^4 (M/\mathrm{M}_\odot)$ $\mathrm{L}_\odot$)[3] requires $M \gtrsim 10^8$ $\mathrm{M}_\odot$. BHs with masses $\gtrsim 10^6$ $\mathrm{M}_\odot$ are commonly referred to as super-massive BHs (SMBHs).

1.2 X-ray emission from AGN

An important discovery dating back to the early days of X-ray astronomy was that X-ray emission is a common property of AGN, with their luminosity in the $2-10$ keV band constituting a considerable fraction

[1] If the width of the observed optical emission lines are due to Doppler broadening, then broad lines indicate large orbital velocities if the irradiated gas clouds are gravitationally bound to the central engine.

[2] In this context, efficiency refers to the percentage of mass that is converted into radiation.

[3] The Eddington limit corresponds to the maximum possible mass of an object that accretes surrounding material such that its gravitational pull is exactly balanced by radiation pressure.

of their bolometric output ($\sim$ 10% for an AGN radiating at $\sim$ 1% of its Eddington limit; Vasudevan & Fabian 2007). In fact, according to X-ray surveys there are more "Type 1" Seyfert galaxies per unit volume emitting in the $2-10$ keV band than those found in surveys conducted in any other wavelength band (Danese *et al.* 1986).

The X-ray flux in AGN shows the fastest variability in any of the wavelength ranges (McHardy 1989), indicating that the X-ray emission originates from a very compact region. Indeed, for variability time-scales $\sim$ 1 h accompanied by a change of the observed source flux by a factor of $\sim$ 2, one could argue that, for an X-ray source undergoing a phase of uniform brightening and/or dimming, its linear dimensions cannot exceed the corresponding light-crossing time $\sim$ 1 lh $\sim$ 10 AU. This order-of-magnitude estimate has recently been confirmed by studies that used gravitational micro-lensing techniques (Chartas *et al.* 2009, Dai *et al.* 2010; Chartas *et al.* 2012) to deduce that the X-ray emitting region in some quasars may be as small as $\sim 10\ R_{\rm g}$[4] which, for a typical SMBH of mass $\sim 10^8\ M_\odot$, corresponds to a region of size $\sim$ 1 AU.

The compactness of the X-ray emitting region in liaison with the fact that a sizeable fraction of the bolometric output of AGN is in the form of X-rays suggests that the X-ray source is located close to the central object. Therefore, detailed X-ray spectroscopy and timing observations are bound to play an important role in understanding the X-ray source physics and geometry, since they provide us with an indirect method to probe the inner-most region in AGN. This may in fact be the only possible way, since direct imaging of this region −which would provide conclusive evidence of the existence of the putative accretion disc as well as reveal the geometry of the emitting region− will probably remain well out of our technological capabilities for the foreseeable future. Indeed, even galaxies at a "modest" distance $\sim$ 1 Mpc would require an angular resolution of $\sim 10^{-2}\ \mu$asec in order to probe regions of size $\sim$ 1 AU.

To first order, the majority of AGN can be characterised by a power-law continuum in the $2-10$ keV range with a photon index $\Gamma \simeq 1.7$ (e.g. Bianchi *et al.* 2009).[5] The origin of this continuum emission is now believed to be a hot "corona" of electrons that inverse-Compton (IC) scatter the [predominantly] optical/UV photons emitted by the accretion disc into the X-ray regime (Sunyaev & Titarchuk 1980). Interestingly, if one assumes the existence of a hot, homogeneous and optically-thin region (the "corona") located above a cold optically thick disc, then the energy coupling between the two[6] requires the Comptonised component to achieve a power-law spectrum with a photon index $\Gamma \simeq 2$, provided almost all of the gravitational power of the disc is dissipated in the "corona" (Haard & Maraschi 1991). This is in agreement with studies that deconvolved the broad "hump", superimposed on the X-ray continuum, that is observed around $\sim$ 30 keV in the X-ray spectra of AGN, thereby obtaining a revised, "intrinsic" power-law photon index $\simeq 1.9$ (e.g. Pounds *et al.* 1990). The restriction of requiring most of the gravitational power to be dissipated into the "corona" can be relaxed by assuming the "corona" is not homogeneous, but composed of a number of discrete

[4] The *gravitational radius*, $R_{\rm g}$, of a spherical object of mass M is defined by $R_{\rm g} = GM/c^2$.

[5] The photon index, Γ, is a parameter in power-law models that assume the flux of a source at energy E (in units of photons per unit time and area) is $\propto E^{-\Gamma}$. As such, a positive photon index indicates the source flux decreases with increasing energy.

[6] This coupling is to be understood in the sense that the dominant cooling mechanism of the "corona" is the Compton up-scattering of low-energy photons produced by the disc, while the hard Comptonised photons contribute to the heating of the latter.

"blobs". Under this assumption, Haardt, Maraschi & Ghisellini (1994) showed the emitted spectrum to be largely independent of the fraction of gravitational power dissipated in the "blobs". In any case, the heating mechanism of the "corona" still remains uncertain. Some possibilities include portions of the accretion flow that are intrinsically hot (e.g. Shapiro, Lightman & Eardley 1976; Narayan & Yi 1994), or that magnetic re-connection creates hot flaring regions above the accretion disc (Nayakshin & Melia 1997; Poutanen & Fabian 1999).

While it is generally agreed that Comptonisation is behind the observed X-ray power-law continuum in AGN, Comptonisation spectra cannot by themselves provide information about the geometry and dynamics of the Comptonising electrons (the "Comptonising cloud"). This allows for different geometrical configurations of the "Comptonising cloud" that can reproduce the observed X-ray power-law continuum (normalisation plus index). For instance, according to the "disc-corona" model mentioned previously, the "Comptonising cloud" is composed of a hot, low-density plasma which may either be uniform or patchy. An alternative explanation that can also reproduce a power-law continuum with an index that it consistent with observation was proposed by Reig, Kylafis & Giannios (2003). This model assumes the "Comptonising cloud" to be composed of mildly relativistic electrons moving along the axis of a jet with a uniform magnetic field that is perpendicular to the accretion disc.

Apart from the X-ray continuum and broad hump at ~ 30 keV, there are several other observational features in the X-ray spectra of AGN. One such feature is a characteristic excess of "soft" X-rays ($\sim 0.5 - 2$ keV) with respect to the intrinsic power-law emission (the so-called "soft excess"; Arnaud *et al.* 1985, Bianchi *et al.* 2009). Although the origin of the "soft excess" remains uncertain, the main competing models that have been proposed in an attempt to explain this feature include: 1) Reflection from the inner regions of an accretion disc (Miniutti & Fabian 2004, Crummy *et al.* 2006), and 2) emission from a hot "skin" on top of an accretion disc that Compton up-scatters low-energy photons from the disc into the "soft" X-ray regime (Done *et al.* 2012; Gliozzi *et al.* 2013).

A further major observational result from the study of AGN X-ray spectra is the presence of emission lines at energies above $\gtrsim 2$ keV, the more prominent of which is centered at ~ 6.4 keV and exhibits an equivalent width (EW)[7] clustered around $50 - 120$ eV (Bianchi *et al.* 2009). This feature is thought to be Kα (which corresponds to a $2p \rightarrow 1s$ electronic transition) emission from neutral Fe, while the rest of the emission lines are believed to correspond other to electronic transitions of neutral Fe (such as Kβ), as well as from ionised species of Fe (e.g. Fe XXV and Fe XXVI). The presence of strong Fe emission is qualitatively expected due to its abundance as a heavy element as well as its high fluorescent yield.[8] In fact, it turns out that the element with the highest product of fluorescent yield and abundance is Fe by a factor of ~ 5.

[7]The EW (typically measured in units of eV or Å) is a measure of the strength of a spectral line, with respect to the underlying continuum emission. It is formally defined as being equal to the width of a rectangle with a height equal to the level of continuum emission, such that the area of the said rectangle is equal to that of the spectral line. As such, a spectral line with a low EW value will not be a prominent feature in the spectrum, while a high EW value indicates the line will be present in the spectrum as a strong feature above the underlying continuum.

[8]An element's fluorescent yield is defined as the probability that a vacancy in a particular atomic shell leads to a radiative transition, rather than the ejection of an Auger electron.

1.3 The "illuminated disc" hypothesis

In an attempt understand the origin of the observed emission lines in the X-ray spectra of AGN, George & Fabian (1991) considered the following problem: What happens when cold, optically thick material is illuminated by an X-ray continuum source? In order to study this complicated problem in a quantitative way, the authors considered a simplified version of it in which only the reflected continuum and Fe K-shell fluorescent photons emerging from a "cold" slab irradiated by an external X-ray source are considered. In order to compute the consequences of this scenario, the authors made the following assumptions:

- The neutral matter is in the form of a homogeneous slab with a sharp boundary, i.e. the slab is assumed not to possess an atmosphere.
- The dominant light-matter interaction processes in the slab are photoelectric absorption and electron scattering.
- The matter within the slab is assumed to be "cold" ($T \leq 10^6$ K), such that the elements responsible for photoelectric absorption at energies ≥ 1 keV can be considered to have filled L- and K-shells. Furthermore, the Fe atoms are assumed to have filled M-shells as well.
- The illuminating X-ray continuum is assumed to be described by a power-law model of the form $N(E_0) \propto E_0^{-\Gamma}$ (in photons per keV), where $1 \leq E_0 \leq 100$ keV and $1.2 \leq \Gamma \leq 2.3$.

Based on these assumptions, the authors computed the expected "reflection spectra" of the illuminated slab using numerical methods. Two different geometries were considered − a semi-infinite slab and a disc. Clearly, the latter case is of direct interest to the problem of X-ray emission in AGN assuming the existence of the putative accretion disc. Their results, shown in Figure 1.1, are in the form of "reflected" and "composite" spectra (directly observed plus reflected components) from a flat, non-rotating disc illuminated by an isotropic X-ray source characterised by a photon index $\Gamma = 1.7$ and located at a height h above the centre of the disc. The disc is assumed to extend from an inner radius $r_{\rm min} = 0$ to an outer radius $r_{\rm max} = 100h$. Separate curves are shown for various inclination angles i, relative to the normal of the slab.

The main characteristics of the computed spectrum are:

- In the $\sim 1 - 7$ keV energy band ("soft" X-rays) the reflection component rises with increasing energy. This is due to photoelectric absorption becoming less prominent with increasing energy.
- The Fe Kα and Kβ fluorescent lines at 6.4 keV and 7.1 keV respectively are clearly visible as strong emission lines, with $\mathrm{EW}_{\mathrm{K}\alpha} \sim 150$ eV for $i \lesssim 45°$.
- A Fe K-shell absorption edge is seen at ~ 7 keV. This is understood as the result of an increase in the absorption cross-section for photons with energies greater than or equal to the binding energy of a Fe K-shell electron.

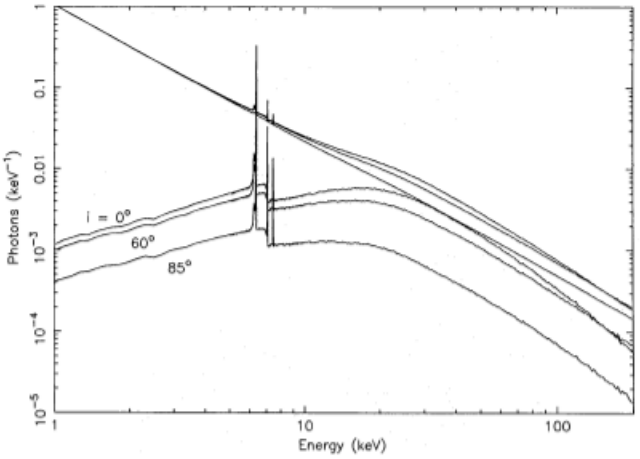

FIGURE 1.1: "Reflected" and "composite" spectra for a flat, optically thick, non-rotating circular slab illuminated by an isotropic source of primary X-rays located at a height h above the centre. The spectra shown are for a disc with a radius of $100h$ and a power-law incident spectrum with $\Gamma = 1.7$, viewed at inclination angles $i = 0°$, $60°$ and $85°$. From George & Fabian (1991).

- In the $\sim 20 - 100$ keV energy band ("hard" X-rays) a characteristic "hump" (the co-called "Compton reflection hump", or "Compton hump" for brevity) is observed in the "composite" spectrum. Since the absorption cross-section for such high energy photons is negligible, this feature is due to Compton scattering. Indeed, it is expected that high energy (> 100 keV) photons will loose a considerable amount of energy as they escape from the slab upon being scattered.[9] This results in a characteristic "hump" in the observed "composite" spectrum.

At energies > 100 keV the "reflected" spectrum decreases with increasing energy, as the probability of such high energy incident photons interacting with the matter in the slab becomes negligible (in effect, the very high energy photons pass right through the slab).

More recently, Ross & Fabian (2005) considered the same problem, albeit with less restrictive assumptions that allowed them to investigate a broader part of the parameter space associated with the problem of X-ray reflection. The authors included fully and partially ionised species of C, N, O, Ne, Mg, Si and S in their calculations, all of which were assumed to have solar abundances, except Fe whose abundance was allowed to vary. Furthermore, the matter in the disc was allowed to have a variable degree of ionisation, quantified by the so-called "ionisation parameter" $\xi = 4\pi F_{\rm tot}/n_{\rm H}$, where $F_{\rm tot}$ is the total illuminating flux and $n_{\rm H}$ is the number density of H.[10] The disc was assumed to be in the form of a slab of uniform number density $n_{\rm H} = 10^{15}$ cm^{-3} and Thomson optical depth ≥ 5. Moreover, the illuminating X-ray source was modelled as having a cut-off power-law spectrum with a flux density of the form $F_E \propto E^{-\Gamma+1}e^{-E/E_{\rm c}}$ (in units of s^{-1} cm^{-2}), where $E_{\rm c} = 300$ keV.

[9] In particular, for a single-scattering event the average energy released from a 100 keV photon to a non-relativistic electron due to Compton scattering is ~ 20 keV.

[10] As such, a high value of ξ results in a higher degree of ionisation and vice-versa.

The values of the ionisation parameter ξ, photon index Γ and Fe abundance $A_{\rm Fe}$ (relative to its solar value) were varied independently in order to investigate their effect on the "reflection" spectra. Three such computed spectra for different values of ξ, an incident spectrum of $\Gamma = 2.0$ and Fe with solar abundance (i.e. $A_{\rm Fe} = 1$) are shown in Figure 1.2.

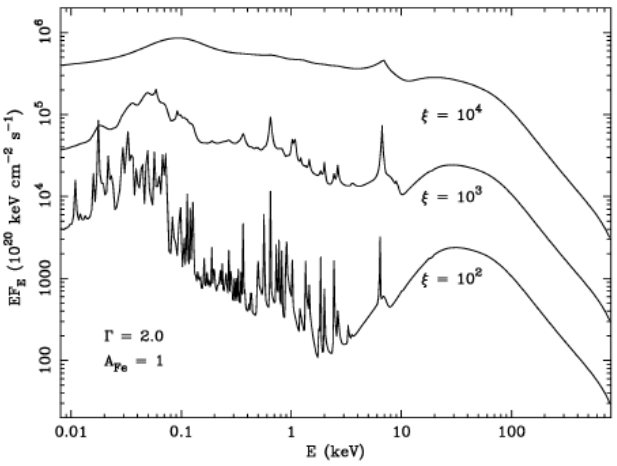

FIGURE 1.2: "Reflected' spectra for three values of the ionisation parameter, with $\xi = 10^2$ (bottom curve), 10^3 and 10^4 erg s^{-1} cm (top curve). The incident power-law spectrum has $\Gamma = 2.0$, and Fe has solar abundance. From Ross & Fabian (2005).

The ionisation parameter clearly has a marked effect on emission and absorption features in the "reflected" spectrum. The main features of the spectra shown in Figure 1.2 are:

- Contrary to the results obtained by George & Fabian (1991), the reflected spectrum increases with decreasing energy in the "soft" ($\sim 0.01 - 1$ keV) band due to brehmsstrauhlung emission from ionised elements as well as a multitude of emission lines. These lines are especially prominent for low values of ξ.
- In each case, the Fe Kα line is prominent. However, as ξ increases the line becomes broadened. This is because, for high values of ξ, there is a significant portion of the upper layer of the disc that is ionised. Since the Fe Kα photons originate mostly from the deeper layers of the disc that are less ionised, the fluorescent photons escaping from the disc get Compton up-scattered and broadened by the energetic electrons in the upper ionised layer.
- As in Figure 1.1, the "Compton hump" is observed in the $\sim 20 - 100$ keV energy band.

1.3.1 Strong gravity effects on the Fe Kα line

Under the assumption that the fluorescent Fe Kα line originates from material close to the central object that powers AGN, one might argue that observed line emission comes from the inner parts of the putative accretion disc. The consequences regarding the shape of an observed Fe Kα line originating from cold

material orbiting close to a BH while being illuminated by an X-ray source were studied by Fabian *et al.* (1989) who made the following assumptions:

- The cold, reflecting gas is in the form of an accretion disc with Keplerian velocities.
- Power-law X-ray emission originates above and below the central parts of the disc within $\sim 5R_{\rm g}$.
- There is a Schwarzschild (i.e. non-rotating) BH at the centre of the accretion disc.

Under these assumptions, the authors computed the expected line profiles of the Fe Kα line for different inner and outer disc radii ($r_{\rm in}$ and r_0, respectively) as well as inclination angles, i. A further parameter q is also introduced and is defined as the index of the line emissivity, which was assumed to be $\propto r^q$, where r is the radial distance as measured from the centre of the disc.[11] Several examples of the computed line profiles are shown in Figure 1.3.

In most cases the Fe Kα line profile exhibits an extended "red wing", which is the result of photons being redshifted upon escaping from the gravitational well of the BH. For $i \neq 0$, the line profile exhibits a characteristic "double-horned" shape, which is a product of the Doppler effect due to the orbital motion of the illuminated gas. However, the "blue horn" is always more prominent than the "red" one, owing to the effect of relativistic Doppler boosting. A similar work was performed later by Laor (1991), who considered the effect of a *rotating* (i.e. Kerr) BH on the line profiles.

Evidently, the detection and study of the overall shape of the Fe Kα line is of primary importance. The width of the line will allow us to infer the rotational velocities of the emitting gas − the broader the line, the closer it should orbit to the central object (assuming Doppler broadening). In addition, the presence of a prominent "red wing" would be, in light of the preceding discussion, an indication of general-relativistic (GR) effects. Both of these characteristics could thus be used as indirect evidence the existence of a BH.

[11] The emissivity of a body (in this case the surface of the disc) is defined as the ratio of its radiated energy to the corresponding energy radiated by a black-body of the same temperature. Since the amount of energy radiated by the surface of the disc depends on the radiative flux it receives from the X-ray continuum, the emissivity is expected to be $\propto r^q$. In the case of Euclidean geometry a value of $q = -2$ is expected, although close to a BH the continuum photons will follow curved paths that results in a stepper slope, i.e. $q < -2$.

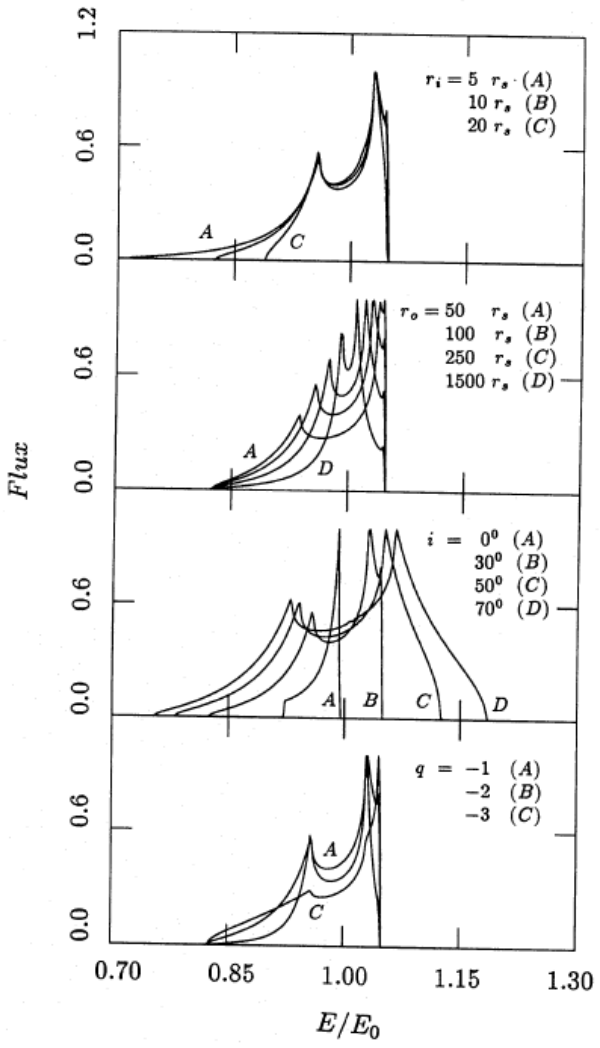

FIGURE 1.3: Computed Fe Kα line profiles assuming cold, reflecting gas in the form of a disc with Keplerian velocities that is close to a BH and illuminated by an X-ray continuum source located above and below the disc. When not specified, $r_{\rm i} = 10r_{\rm s}$, $r_0 = 100r_{\rm s}$, $i = 30^\circ$ and $q = -2$. From Fabian *et al.* (1989). It is noted that the symbol $r_{\rm s}$ in the figure represents the Schwarzschild radius, which is defined as twice the gravitational radius $R_{\rm g}$.

1.3.2 The case of MCG−6-30-15

MCG−6-30-15 is a spiral galaxy that hosts a "Type 1" Seyfert nucleus. It has an observed red-shift of $z = 0.008$ which, for a standard Λ-CDM Cosmology with $H_0 = 73$ km s^{-1} Mpc^{-1}, $\Omega_{\rm M} = 0.27$ and $\Omega_\Lambda = 0.73$, corresponds to a luminosity distance of 35.8 Mpc.[12] In 1995, Tanaka *et al.* reported the first ever observation (obtained with the *ASCA* X-ray satellite) of an asymmetric Fe Kα emission line with a broad "red wing" in MCG−6-30-15. Their data are shown in Figure 1.4. The amount of broadening of the line suggests orbital velocities $\sim 10^5$ km s^{-1} (assuming Doppler broadening), while the data are consistent with the line arising from a region between 1.5 and $5R_{\rm g}$ from the centre of a BH.

More recently, MCG−6-30-15 has been observed by both *XMM-Newton* (Fabian *et al.* 2002) as well as *Suzaku* (Miniutti *et al.* 2007), yielding higher quality X-ray spectra. In both cases a broad Fe Kα line is observed (see Figure 1.5).

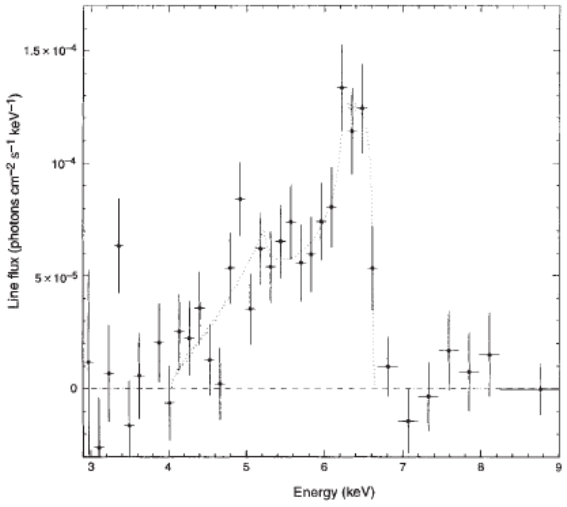

FIGURE 1.4: The line profile of Fe Kα in the X-ray emission from MCG−6-30-15. The emission line is broad, with a full width at zero intensity that corresponds to $\sim 10^5$ km s^{-1}, assuming Doppler broadening. There is a marked asymmetry at energies lower than the rest-energy of the emission line (6.35 keV at the source red-shift of 0.008). The dotted line shows the best-fit Fabian *et al.* (1989) line profile. From Tanaka *et al.* (1995).

However, the origin of the Fe Kα line in MCG−6-30-16 still remains uncertain. For instance, using available *Suzaku* data, Miller, Turner & Reeves (2008) proposed an alternative explanation regarding its origin. According to them, the broad Fe Kα line observed in MCG−6-30-15 can be explained by assuming the existence of absorbing material, in the form of a clumpy disc wind, along the line of sight. Their model suggests the Fe Kα line is intrinsically narrow, but appears broadened due to the combination of distant reflection and the effect of a variable covering fraction of absorption of the primary continuum source (see Figure 1.6).

[12] This information is taken from the NASA/IPAC Extragalactic Database (NED) which can be found at http://ned.ipac.caltech.edu/.

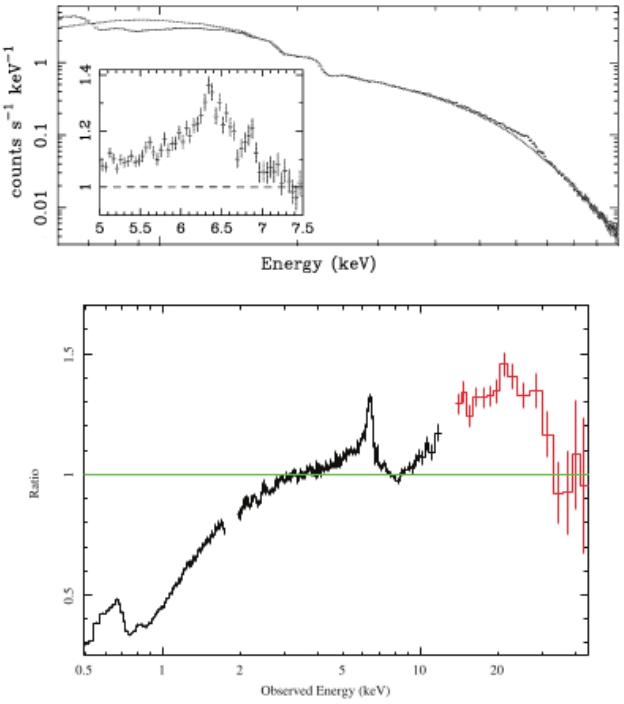

FIGURE 1.5: *Top panel*: *XMM-Newton* spectrum of of MCG−6-30-15. The inset panel shows a close-up of the Fe Kα line. From Fabian *et al.* (2002). *Bottom panel*: *Suzaku* spectrum of MCG−6-30-15. The ratio plot shows the main spectral components which are the power-law continuum, absorption below $\sim$ 3 keV and a strong smeared reflection component comprising the broad Fe Kα line and "Compton hump". From Miniutti *et al.* (2007).

There are thus ambiguities as to the origin of the Fe Kα line in MCG−6-30-15 − is it produced in the inner-most regions of an accretion disc, owing its features to effects of strong gravity, or is it produced by reflectors distant to the central source and artificially broadened due to different layers of variable obscuration levels? Since both models can explain the observed spectral characteristics of the line, further observational properties need to be tested against them. This can be done by X-ray variability studies. I will thus focus my attention in the following sections on how one studies X-ray variability in order to constrain the physics and geometry of the X-ray emitting region in AGN.

1.4 X-ray variability

As mentioned in §1.2, the X-ray spectra of AGN show rapid variations on relatively short time-scales. There have been several attempts to provide a theoretical framework for explaining the physical mechanism that gives rise to this variability, although the details are not known at the present stage. Even so, if the "illuminated disc" hypothesis is true, then, whatever the nature of the X-ray continuum may be, if the reflector and source are close then [almost] any variation in the continuum should be mimicked in the "reflected" emission from the disc. Geometry evidently plays a crucial role in how the disc will "respond" to a sudden variation of the incident photons from the illuminating X-ray continuum source. For instance,

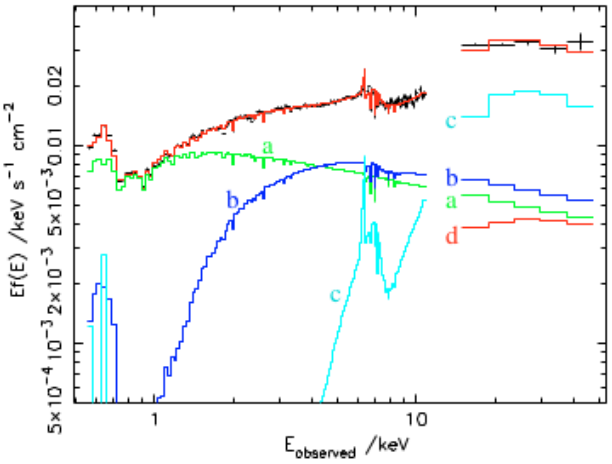

FIGURE 1.6: Illustration of the model by Miller, Turner & Reeves (2008). The upper curve shows the model fitted to the mean *Suzaku* spectrum. The three emission components are shown as (a) primary directly-viewed power-law; (b) partially-covered power-law; (c) reflection; (d) the expected contribution of the cosmic X-ray background to the *Suzaku* band. From Miller, Turner & Reeves (2008).

the source might be point-like and along the axis of symmetry, orbiting close or far from the disc, or even extended. In each case, the "response" of the disc would be different.

In practice, information regarding the variability properties of a given source is obtained by studying its so-called *light-curve*, which is a collection of measurements of its flux obtained at regular time intervals. Depending on the sensitivity of the recording apparatus one can obtain light-curves of the same source that correspond to emission in different energy bands. The study of temporal correlations between light-curves in energy bands which are thought to be representative of the X-ray continuum and "reflected" emission has been the subject of an active field of research during the past few years. The aim of those studies is first of all to determine whether or not the two components are correlated (as one would expect if the "illuminated disc" hypothesis is correct), and secondly to investigate how this correlation −which is expected manifest in the form of temporal delays (or time-lags) between the two light-curves− is related to the physics and geometry of the X-ray emitting region.

Past works have so far assumed that the $0.5 - 1.5$ keV band (henceforth the "Soft" band) represents "reflected" emission, while the $2 - 4$ keV band (henceforth the "Continuum" band) represents emission from the primary X-ray continuum source. This is because, according to the ionised disc reflection model by Ross & Fabian (2005), it is expected that in the "Soft" band the "reflection" component contributes the most significant fraction of the total observed emission, while in the "Continuum" band the "reflection" component is minimal (see Figure 1.2).

1.4.1 Observed AGN time-lag spectra

As mentioned previously, the detection and study of time-lags between various X-ray energy bands is widely used as a diagnostic of the X-ray emission mechanism and source geometry in AGN (e.g. Papadakis, Nandra & Kazanas 2001; McHardy *et al.* 2004; Arévalo *et al.* 2006; Arévalo, McHardy & Summons 2008; Sriram, Agrawal & Rao 2009). In AGN it is usually observed that high-energy band variations are delayed with respect to lower energy band variations (henceforth referred to as "positive" time-lags) at time-scales $\gtrsim 10$ ks, and their origin is still ambiguous − they are expected in standard Componisation scenarios (e.g. Nowak *et al.* 1999; Reig, Kylafis & Giannios 2003), in the sense that high-energy photons are expected to undergo more scatterings as they move through the "Comptonising cloud" than lower-energy photons, but can also be caused by other mechanisms. For instance, Kotov, Churazov & Gilfanov (2001) argued that "positive" time-lags can arise by inward propagation of perturbations in the accretion flow that manifest themselves on diffusive time-scales.

Detections of low-energy band variations being delayed with respect to higher energy band variations (henceforth referred to as "negative" time-lags) were first reported for the "Type 1" AGN Mrk 766 (Markowitz *et al.* 2007) and Ark 564 (McHardy *et al.* 2007). The first robust detection of "negative" time-lags was reported by Fabian *et al.* (2009) for the Type 1 AGN 1H 0707-495. The origin of "negative" time-lags is even less clear, although Fabian *et al.* (2009), Zoghbi *et al.* (2010) and Zoghbi, Uttley & Fabian (2011) favour the interpretation that they arise from reflection by matter lying close to a BH.

Vaughan, Fabian & Nandra (2003) were the first to estimate the time-lag spectrum of MCG−6-30-15 by using light-curves with a large time bin of 100 s.[13] "Negative" time-lags were first detected in the "Soft vs Continuum" time-lag spectrum of MCG−6-30-15 by Emmanoulopoulos, McHardy & Papadakis (2011; henceforth EMP11), who used long *XMM-Newton* observations. Their results are shown in Figure 1.7, alongside corresponding spectrum of another "Type 1" AGN, Mrk 766. In both cases, the time-lags are plotted as a function of frequency, which corresponds to the inverse of the time-scale.

Even though the "Soft vs Continuum" time-lag spectrum is predominantly positive at $< 5 \times 10^{-4}$ Hz, it shows a curious minimum of ~ -20 s at $\sim 10^{-3}$ Hz. EMP11 argued that the "Soft vs Continuum" time-lag spectrum of MCG−6-30-15 is composed out of two separate terms; a "reflection" component and a "power-law" in order to model the "positive" time-lags at low frequencies. Furthermore, EMP11 concluded that the observed time-lags suggest the size of the reflector to be $\lesssim 6R_{\rm g}$ (assuming a SMBH mass of 5×10^6 $M_\odot$; McHardy *et al.* 2005).

Time-lag spectra have since been estimated for a number of Type 1 AGN (De Marco *et al.* 2013). As seen in Figure 1.8, the estimated time-lag spectra have similar profiles for each source, even though they span 2.5 orders of magnitude in estimates of their BH masses ($M_{\rm BH}$). If "negative" time-lags are the result of

[13] The time bin of a light-curve corresponds to the time elapsed between two consecutive measurements of the source flux. Since measuring time-lags between two light-curves corresponds to measuring the phase shift between their sinusoidal components, the maximum frequency that can be probed for a time bin $\Delta t_{\rm bin}$ is expected to be $\sim 1/\Delta t_{\rm bin}$.

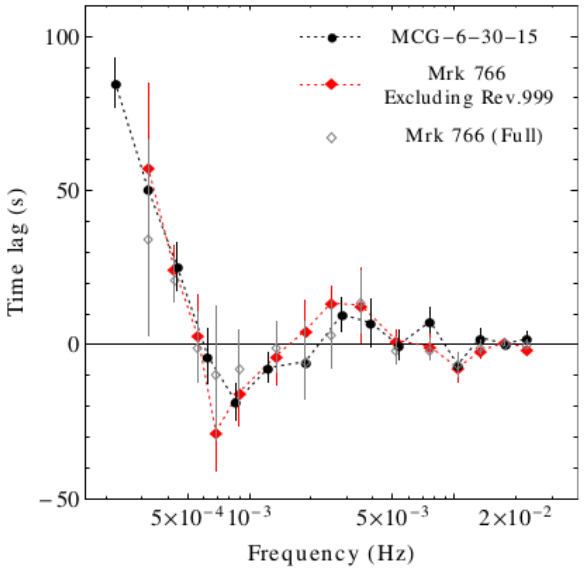

FIGURE 1.7: The "Soft vs Continuum" time-lag spectra of MCG−6-30-15 (filled black dots) and Mrk 766 (filled red and open grey diamonds). The dotted lines joining the points are purely intended to guide the eye. From EMP11.

reverberation, then one would expect their value to scale linearly with $M_{\rm BH}$. This can be deduced by the following argument: Assuming the "negative" time-lags τ are the result of reflecting material close to a BH, they are expected to be proportional to the light-crossing time the magnitude of which is dictated by $R_{\rm g} \propto M_{\rm BH}$. Therefore, one would expect that $\tau \propto R_{\rm g} \propto M_{\rm BH}$. A strong linear $\tau - M_{\rm BH}$ correlation has indeed been reported by De Marco *et al.* (2013) for sources with the highest negative time-lag detection significance.

1.4.2 The main scientific objective of the present work

Estimating time-lags from the temporal correlations between different AGN X-ray light-curves has so far been limited to studying the the "Soft" and "Continuum" energy bands. However, the origin of the "Soft" band emission remains debatable. It is thus questionable whether the observed AGN time-lag spectra may be interpreted within the context of the "illuminated disc" hypothesis.

The objective of the present work is (a) to study, for the first time, the variability between the Fe Kα line and the "Continuum" band, and (b) attempt to further constrain the "Soft vs Continuum" time-lag spectrum that has already been determined for MCG−6-30-15. The reason I chose this particular source is because it is a bright X-ray source and was historically the first AGN for which a broad Fe Kα emission line was detected. Furthermore, MCG−6-30-15 has been observed several times by various X-ray satellites (e.g. *ASCA*, *Suzaku* and *XMM-Newton*), and thus there are lots of available data on this source. To this end, I obtained all available *Suzaku* and *XMM-Newton* light-curves in the $5 - 6.6$ keV energy band (henceforth, the "Iron-line" band) which is expected to contain the majority of Fe Kα emission in the X-ray spectrum

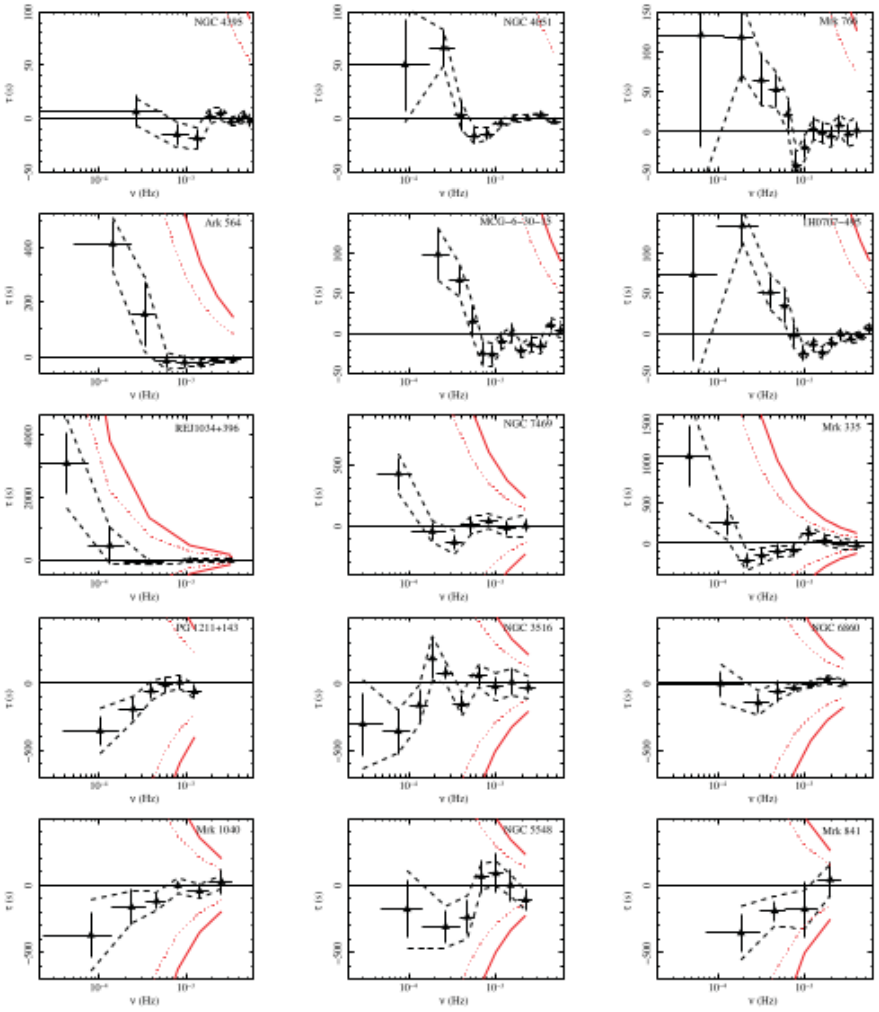

FIGURE 1.8: Time-lag spectra of sources with detected negative time-lags at a $> 2\sigma$ confidence level, in order of increasing mass (from top left to bottom right). The dashed curves correspond to 1σ confidence levels. The continuous red curves limit the range $\tau = [-1/2\nu, 1/2\nu]$ of allowed time-lag values τ at each frequency $\nu = \omega/2\pi$, while the red dotted curves mark the standard deviation of of a uniform distribution defined on the same interval of time-lag-permitted values. From De Marco *et al.* (2013).

of MCG−6-30-15 (see Figures 1.4 and 1.5), as well as in the "Soft" and "Continuum" bands. This is also the first time that *Suzaku* light-curves have been used in order to estimate time-lag spectra.

The rest of my thesis is structured as follows: In Chapter 2 I discuss the specifics of the data reduction. In Chapter 3 I introduce the subject of Time Series Analysis, which provides the statistical tools needed for quantitatively studying the temporal correlations between the different light-curves I obtained. Finally, in Chapter 4 I present the results of the data analysis and draw my conclusions in Chapter 5.

Chapter 2

Observations and Data Reduction

2.1 The Suzaku observatory

Suzaku (initially named *ASTRO-EII* before launch) is a Japanese X-ray satellite launched on 10 July 2005 as part of a joint Japanese-US mission and is sensitive in the $0.3-600$ keV range. Its objective is to observe a wide variety of X-ray sources. The satellite moves in a near circular orbit with a period of ~ 96 min around Earth and an apogee of 568 km.

The scientific payload of *Suzaku* consists of three distinct co-aligned scientific instruments. The first instrument consists of four X-ray sensitive imaging CCD cameras (X-ray imaging spectrometers, or XIS), three of which are "front-illuminated". The "front illuminated" ("back-illuminated") XIS are characterised by a bandpass of $0.4-12$ keV ($0.2-12$ keV), effective area of ~ 340 cm^2 (~ 390 cm^2) and ~ 150 cm^2 (~ 100 cm^2) at 1.5 keV and 8 keV, respectively. Each XIS is located at the focal plane of an X-ray telescope (XRT). The second instrument is the non-imaging collimated hard X-ray detector (HXD), which extends the bandpass of the observatory to the $10-600$ keV range. The third instrument is the co-called X-ray spectrometer (XRS) and is no longer operational.

All the instruments on *Suzaku* operate simultaneously. Each one of the co-aligned XRTs features an X-ray mirror with an angular resolution of $\sim 2'$. The four XIS (named XIS0, 1, 2 and 3) have a large ($\sim 18' \times 18'$) field of view (FOV) and a moderate spectral resolution (~ 130 eV at 6 keV). Each CCD camera has a single CCD chip with an array of 1024×1024 square pixels each having a side of 24 μm (the size of the CCD is 25 mm $\times$ 25 mm). In November 2006 a large amount of leak charge that could not be suppressed appeared on XIS2, resulting in the termination of the usage of said detector for scientific observations. Thus three XIS detectors (XIS0, XIS1 and XIS3) are currently usable.

Each CCD is read out at regular intervals of 16 s. In general, each pixel stores three numbers for each recorded photon; its energy, location (in terms of (x, y) coordinates on the CCD) and time of arrival.

Hence, one can extract the following information regarding the source target that is being observed each time:

- The source light-curve, which corresponds to the number of photons recorded per unit interval. Light-curves can in principle be extracted for different energy bands by only choosing photons that have been recorded in the energy band of interest.
- The source image contains the total number of photons (or counts) that were collected over the entire available energy range during the total observing time.
- The source spectrum, which corresponds to the total observed count-rate as a function of energy.

The HXD has an effective area of ~ 160 cm^2 and ~ 260 cm^2 at 20 keV and 100 keV respectively, as well as a field of view actively collimated to $4.5^\circ \times 4.5^\circ$. At energies $\lesssim 100$ keV, an additional passive collimation further reduces its FOV to $\sim 34' \times 34'$. The HXD time resolution is 61 μs. Since the energy bands of interest to the present work are confined to the energy range $0.5 - 6.6$ keV, I did not use data from the HXD.

2.2 Observations of MCG−6-30-15 with Suzaku

MCG−6-30-15 has been observed four times by *Suzaku*, once on August 2005 with an on-source exposure time ~ 47 ks, and three times on January 2006 with significantly longer on-source exposure times (~ 140, 98 and 97 ks, respectively). More detailed information regarding the four observations are listed in Table 2.1. Columns 1, 2, 3 and 4 list the observation number, *Suzaku* identification number of each observation, date at which the observation started (in a YYYY-MM-DD format) and total exposure time (or "on-source exposure") in units of ks, respectively. I downloaded all publicly available data files for each observation from NASA's HEASARC (High Energy Astrophysics Science Archive Research Center) website.[1]

TABLE 2.1: *Suzaku* observations of MCG−6-30-15.

Observation #	ID	Obs. date	Exp. time (ks)
Obs. 1	100004010	2005-08-17	46.7
Obs. 2	700007010	2006-01-09	143.2
Obs. 3	700007020	2006-01-23	98.5
Obs. 4	700007030	2006-01-27	96.7

2.3 Data reduction

In order to reduce and manipulate the available *Suzaku* data I downloaded and installed "HEASoft", which is a publicly available software provided by HEASARC and constitutes a unified release of the "FTOOLS" and

[1]The HEASARC website can be found at http://heasarc.gsfc.nasa.gov/.

"XANADU" software packages. FTOOLS is a general package used to manipulate data files from satellites which are available in a "FITS" file format. XANADU is a software package that comprises high-level, multi-mission tasks for X-ray astronomical data analysis.

2.3.1 "Cleaning" the "raw" event files

Not all of the "raw" *Suzaku* event files contain usable data. For instance, when the satellite enters the so-called "South Atlantic Anomaly" (SAA) −an area where the Earth's inner Van Allen radiation belt comes closest to its surface− the count-rate recorded by the CCDs gets contaminated by radiation disassociated with the target source. Furthermore, as the satellite remains in orbit while observing a certain target, the Earth may get in its FOV, or its sunlit limb. There are many other effects that will cause contamination of an observed target's count-rate, some of which depend on the satellite itself, such as flickering pixels and artificial charge injection of the CCD pixels for the purpose of calibration.

It is customary for mission-specific data reduction software to deploy certain "screening" criteria, in the sense that, starting from a "raw" event file of a certain observation that includes the full recorded data, only those data that satisfy certain conditions are kept for the subsequent analysis. The resulting event files, after the process of screening has been applied, are referred to as "cleaned" event files. The "raw" *Suzaku* event files that I used were "cleaned" using the FTOOLS "aepipeline" command, which deploys standard screening criteria used for *Suzaku* as described in Chapter 6 of the *Suzaku ABC guide*.[2]

2.3.2 Extracting the light-curves

Using the "cleaned" event files, I proceeded to create images for each observation from the four different *Suzaku* XIS instruments using the FTOOLS "xselect" command. An example of one such image is shown in Figure 2.1, which was recorded by the XIS0 detector for Obs. 2 (the rest of the detector images are similar). The brightness of this image corresponds to a logarithmic scale, which mimics the response of the human eye to visual stimuli. The central source is seen dominates the image in terms of brightness, whereas the bright spots in the corners of the image correspond to ^{55}Fe calibration sources (see Chapter 7 of the *Suzaku ABC guide*).[3]

Since only the central source is of immediate interest, one needs to specify a certain region on the image in order to extract, for instance, a light-curves at a specified energy band. This can be done through the DS9 application[4] by placing a circular region centered at the central source, as shown in Figure 2.1.

[2]The *Suzaku ABC guide* is available at http://heasarc.nasa.gov/docs/suzaku/analysis/abc/.

[3]These calibration sources are necessary in order to convert electronic current, which is what CCD detectors ultimately measure, into energy.

[4]DS9 is an astronomical imaging and data visualisation application.

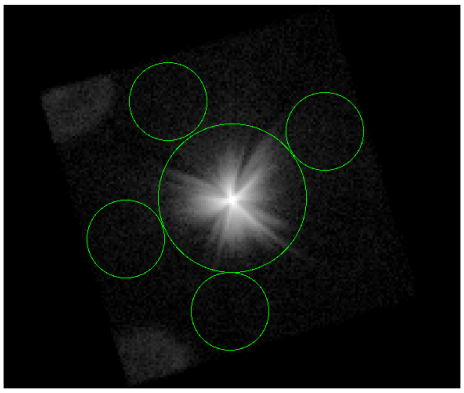

FIGURE 2.1: A "cleaned" event file image extracted from *Suzaku*'s Obs. 2 of MCG−6-30-15, as recorded by the XIS0 detector.

The choice for the radius of the source region is a delicate issue. For instance, one might expect that choosing a circular region with a radius that encompasses the whole image would be sufficient to practically capture the entirety of the source emission. While this is indeed the case, above a certain radius one simply adds background emission that is disassociated with the central source. Therefore, a threshold must be chosen − which radius avoids as much contamination as possible while at the same time contains an appreciable fraction of the intrinsic observed source emission? To a certain degree, this is a technical issue that depends on parameters that are detector-specific. In the case of *Suzaku*, it has been determined (see Chapter 6 of the *Suzaku ABC guide*) that, for a point source, a radius of 250 pixels (260″) encircles 99% of the source flux and is the recommended radius for the central region. This is the radius of the central circular region shown in Figure 2.1.

Even so, the central region still contains a background emission component. The standard procedure for removing that component is to consider additional circular regions that encompass certain parts of the background (i.e. away from the central source). To this end, I created four background regions for each image (one for each observation and XIS detector) and placed them as close as possible to the source region, while their radii were chosen to have a constant value of 131 pixels. The background regions are the smaller, peripheral circles shown in Figure 2.1.

Once the source and background regions on every image were specified, I proceeded to extract light-curves from each region (one source and four background) in the "Soft", "Continuum" and "Iron-line" bands. This was accomplished via the "xselect" command. I then created average background light-curves in every energy band for each observation and each XIS detector, by summing the four background light-curves using the FTOOLS "lcmath" command. The average background light-curves where then subtracted from the corresponding source light-curves (taking into account the difference in area between the background and source regions), which was again done using the "lcmath" command. By using the above procedure I created "background-subtracted" light-curves for each energy band, an example of which is shown in Figure 2.2 in

the case of Obs. 2 (which is the longest of the four observations, as inferred from Table 2.1), as extracted from the XIS0 detector. The time resolution is 5760 s, which corresponds to *Suzaku*'s orbital period.

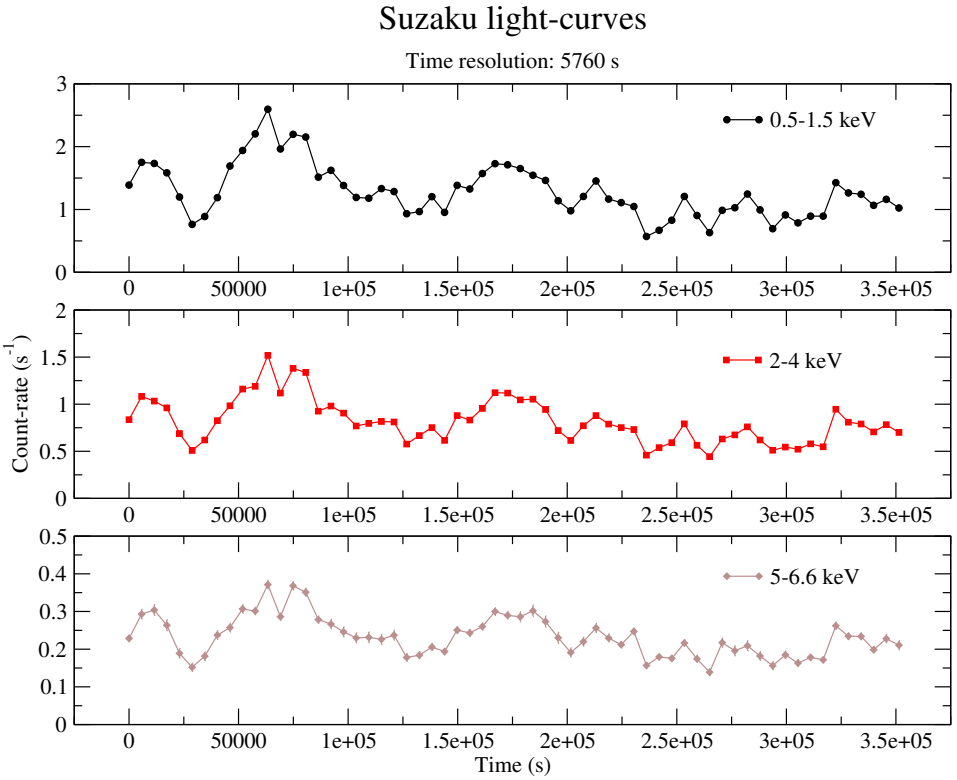

FIGURE 2.2: Background-subtracted light-curves for the "Soft" (black circles), "Continuum" (red squares) and "Iron-line" (brown diamonds) energy bands for Obs. 2 of MCG−6-30-15, as extracted from the XIS0 detector. The time resolution is 5760 s. For the top two panels the error bars are smaller than the size of each data point. The lines joining the data points are put there purely to guide the eye.

The average count-rate is largest in the "Soft" band and smallest for the "Iron-line" band. This is a result of the fact that, as discussed in Chapter 1, AGN intrinsically emit more photons in the former band. Secondly, the XIS detectors on *Suzaku* are more sensitive in this energy band. It is important to note that there is, indeed, variation in the light-curves of MCG−6-30-15 at all sampled time-scales, from the shortest ($\sim$ 6 ks) to the longest ($\sim$ 350 ks). Furthermore, there is a noticeable similarity between variations detected in the different energy bands at all time-scales.

2.3.3 The final 5760 s-binned Suzaku light-curves

The "background-subtracted" light-curves I obtained following the procedures outlined in §2.3.2 are quite similar for each observation between the different XIS detectors. This can be seen in Figure 2.3, where I plot the background-subtracted $0.3 - 10$ keV band light-curves of the different XIS detectors for Obs. 2.

There is a noticeable similarity between the different Obs. 2 XIS light-curves, the exception being the XIS1 light-curve which has systematically recorded higher count-rates than the other three XIS detectors. This

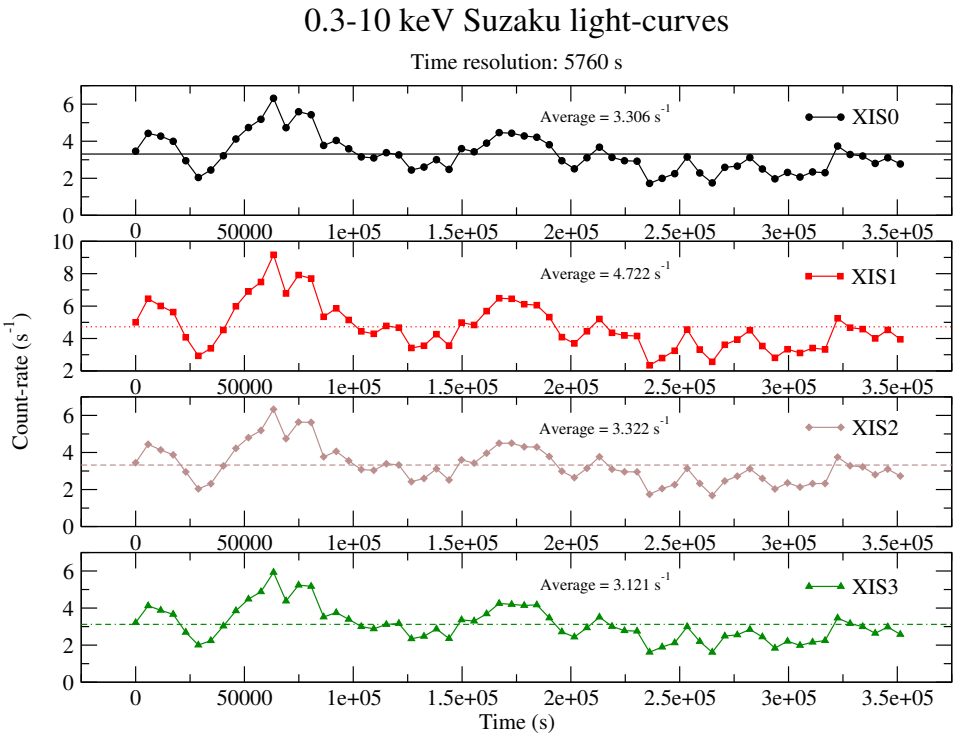

FIGURE 2.3: The four XIS $0.3-10$ keV band light-curves for *Suzaku*'s Obs. 2 of MCG−6-30-15. The black circles, red squares, brown diamonds and green triangles correspond to XIS0, 1, 2 and 3 measurements, respectively. The error bars are smaller than the size of each data point, while the lines joining them are put there purely to guide the eye. For each light-curve there is a corresponding horizontal line that indicates the average count-rate level.

discrepancy is to be expected on the grounds that the XIS1 detector is "back-illuminated", while the rest are "front-illuminated" (see the *Suzaku ABC guide*). Even so, the light-curve shapes seem to be similar. One way to investigate this similarity is to over-plot the four normalised (i.e. with respect to the average count-rate) light-curves, as shown in Figure 2.4.

This similarity now seems even more striking, hence one might assume that the Obs. 2 XIS0-3 light-curves are consistent with each other and thus can be combined. This would be desirable since, by combining the four XIS light-curves, the signal-to-noise ratio (S/N; the fraction of the count-rate error divided by its observed value) is reduced by a factor $\sim 1/\sqrt{4}$. However, this comparison has to be made more rigorous. This can be done by first assuming that the light-curves can indeed be combined − in statistical terms, this corresponds to a so-called *null hypothesis*. If so, the count-rate ratios between any given pair of XIS light-curves should be adequately described by a straight line with a slope ~ 0. These ratios are shown in Figure 2.5.

By fitting the count-rate ratios for the XIS1/XIS0, XIS2/XIS0 and XIS3/XIS0 pairs to a linear model of the form $y = a + bx$, where y is the count-rate ratio and x is the time, I performed a χ^2 minimisation procedure using the "fitexy" FORTRAN subroutine (Press et al. 1992) in order to estimate the parameters a and b and assess the goodness of fit. The results of the fits are listed in Table 2.2; column 1 contains the XIS ratio considered, columns 2 and 3 contain the estimated fit parameters a and b along with their respective

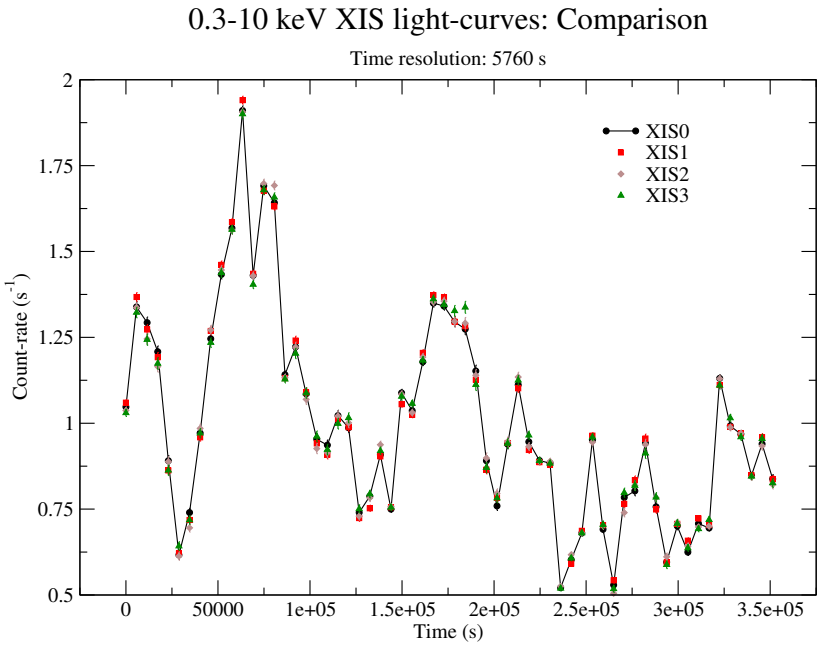

FIGURE 2.4: Comparison between the normalised XIS $0.3-10$ keV light-curves for *Suzaku*'s Obs. 2 of MCG−6-30-15.

errors, column 4 contains the value of the χ^2_d where d is equal to the degrees of freedom ($\equiv$ # of data points minus 2 constraints; DOF) and column 5 contains the probability of the null hypothesis $P_{\rm null}$, i.e. that the data are consistent with the null hypothesis. In the present work I adopted a 5% significance probability threshold, i.e. any result with $P_{\rm null} \geq 0.05$ will be considered as statistically significant (i.e. consistent with the null hypothesis).

TABLE 2.2: Count-rate ratio fits of the XIS continuum light-curves for Obs. 2 of MCG−6-30-15

Ratio	$a \pm \sigma_a$	$b \pm \sigma_b$ (s^{-1})	χ^2_{60}	$P_{\rm null}$
XIS1/XIS0	1.428 ± 0.005	$(6 \pm 27) \times 10^{-9}$	82.36	0.03
XIS2/XIS0	1.004 ± 0.004	$(1 \pm 2) \times 10^{-8}$	62.75	0.38
XIS3/XIS0	0.936 ± 0.004	$(5 \pm 2) \times 10^{-8}$	57.92	0.55

It is found that the count-rate ratios in Figure 2.5 for the XIS0, 2 and 3 detectors can adequately be described by a single average value, since in all cases the slope b is consistent with being equal to zero. This vindicates the initial suspicion, as inferred from Figures 2.3 and 2.4, that the light-curves from the aforesaid detectors can be combined.

The $P_{\rm null}$ values indicate that the fits for the XIS2/XIS0 and XIS3/XIS0 ratios are acceptable, while the fit for the XIS1/XIS0 ratios is not. In particular, since in all cases $b \sim 0$, there does not seem to be statistical trend in the count-rate ratios (e.g. a systematic increase/decrease, or periodic fluctuations). This result suggests a certain amount of scatter of the points about the constant lines $y = a$, which is represented by σ_a. Therefore, including the XIS1 light-curves one would inadvertently introduce a component of variability

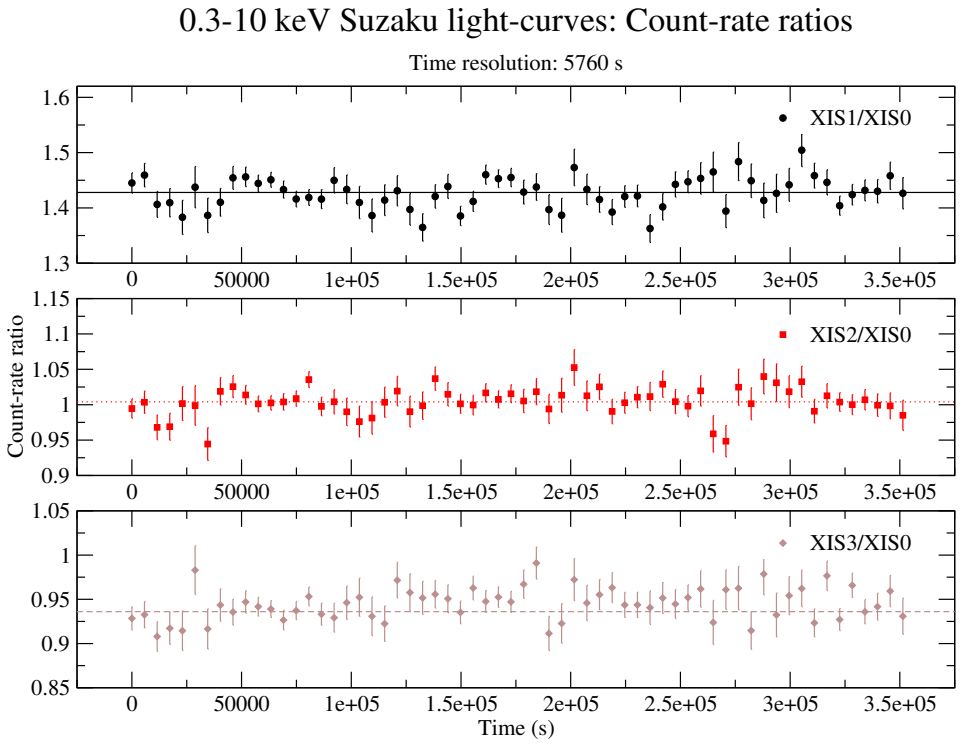

FIGURE 2.5: Count-rate ratios between the $0.3-10$ keV light-curves between the XIS1/XIS0 (black circles), XIS2/XIS0 (red squares) and XIS3/XIS0 (brown driangles) detectors for *Suzaku*'s Obs. 2 of MCG−6-30-15. The continuous, dotted and dashed lines correspond to constant best-fit count-rate values a, as listed in Table 2.2.

that is not intrinsic to the source. Consequently, I combined the XIS0, 2 and 3 light-curves for Obs. 2 of MCG−6-30-15.

Following the exact same procedure as outlined above, I proceeded to test which XIS light-curves can be combined for the rest of the observations. The results of the count-rate ratio fits for the rest of the observations are listed in Table 2.3.

In the case of Obs. 1, all XIS detectors seem to behave in a similar fashion, whereas for Obs. 3 only the XIS0 and 2 detectors seem to do so. Even so, for the purposes of uniformity I decided to combine the XIS0, 2 and 3 light-curves for each observation and every energy band, with the knowledge that, in the case of Obs. 3, a slight component of variability disassociated with the source might be included. The resulting combined light-curves for Obs. 2 are shown in Figure 2.6.

Probing short time-scale variations with Suzaku

The final *Suzaku* light-curves I obtained are binned at 5760 s, contain no missing points and have a high S/N. Hence, they are ideal for the study of correlations between different energy bands at time-scales $\sim 6-350$ ks. However, the *Suzaku* data sets can provide information on significantly shorter time-scales as well by considering 16 s-binned light-curves. Following the exact same procedure outlined in §2.3.2 – 2.3.3,

TABLE 2.3: Count-rate ratio fits of the XIS continuum light-curves for Obs. 1, 3 & 4 of MCG−6-30-15

Obs. 1				
Ratio	$a \pm \sigma_a$	$b \pm \sigma_b$ (s^{-1})	χ^2_{13}	$P_{\rm null}$
XIS1/XIS0	1.77 ± 0.01	$(-4 \pm 2) \times 10^{-7}$	14.77	0.32
XIS2/XIS0	1.060 ± 0.007	$(-3 \pm 16) \times 10^{-8}$	9.13	0.76
XIS3/XIS0	1.021 ± 0.007	$(-2 \pm 1572) \times 10^{-10}$	16.09	0.24
Obs. 3				
Ratio	$a \pm \sigma_a$	$b \pm \sigma_b$ (s^{-1})	χ^2_{36}	$P_{\rm null}$
XIS1/XIS0	1.432 ± 0.007	$(-10 \pm 6) \times 10^{-8}$	73.23	0.00
XIS2/XIS0	0.978 ± 0.005	$(5 \pm 4) \times 10^{-8}$	49.48	0.07
XIS3/XIS0	0.911 ± 0.005	$(5 \pm 42) \times 10^{-9}$	55.81	0.02
Obs. 4				
Ratio	$a \pm \sigma_a$	$b \pm \sigma_b$ (s^{-1})	χ^2_{35}	$P_{\rm null}$
XIS1/XIS0	1.403 ± 0.007	$(2 \pm 6) \times 10^{-8}$	99.26	0.00
XIS2/XIS0	0.988 ± 0.006	$(5 \pm 4) \times 10^{-8}$	40.83	0.23
XIS3/XIS0	0.920 ± 0.004	$(6 \pm 4) \times 10^{-8}$	39.70	0.27

I extracted and combined the 16 s-binned light-curves for the XIS0, 2 and 3 detectors in each of the three energy bands. An example of the resulting Obs. 2 light-curves is shown in Figure 2.7.

The main disadvantage of the 16 s-binned *Suzaku* light-curves compared to the 5760 s-binned ones is that they are not continuous, but rather contain a series of segments separated by gaps. The data segments have a duration $\sim 1 - 3$ ks. Furthermore, the S/N ratio for the 16 s binned light-curves is considerably lower compared to the 5760 s-binned ones (see Figures 2.2 and 2.7 for comparison). Hence Poisson (or counting) noise is expected to cause inevitable complications to any attempt of studying correlations between the 16 s-binned *Suzaku* light-curves at short time-scales ($\lesssim 200$ s).

2.4 The XMM-Newton observatory

XMM-Newton (X-ray Multi-Mirror Mission - Newton; originally known as the *High Throughput X-ray Spectroscopy Mission*) is an orbiting X-ray observatory launched by the European Space Agency (ESA) on December 10 1999. It was placed in a highly eccentric ~ 48 h orbit with a perigee of $7,000$ km and an apogee of $114,000$ km. *XMM-Newton* is sensitive in the $0.1 - 15$ keV range.

XMM-Newton's payload includes:

- Three European Photon Imaging Cameras (EPIC), which are CCD cameras for X-ray imaging, photometry and moderate resolution spectroscopy. Of those three cameras, two belong to the EPIC-MOS category, and one to the EPIC-pn one. The EPIC cameras are characterised by a bandpass of $0.5 - 12$ keV, a FOV $\sim 30'$, a timing resolution of 1.75 ms, a spectral resolution of ~ 70 eV at 1 keV

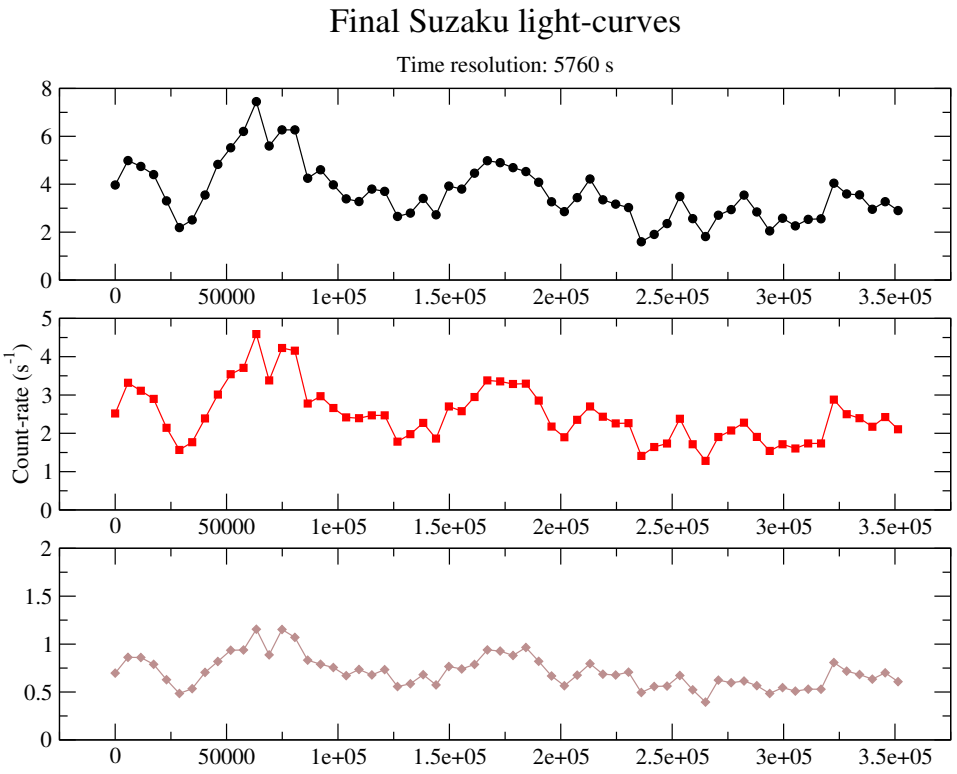

FIGURE 2.6: The final, combined XIS0, 2 and 3 light-curves for *Suzaku*'s Obs. 2 of MCG−6-30-15. The black dots, red squares and brown diamonds correspond to data points for the Soft, Continuum and Iron-line energy bands respectively. The time resolution is 5760 s, while an absence of error bars indicates their size is exceeded by the size of the points.

and $\sim$ 150 eV at the energy of the Fe Kα line and an effective area of 922 cm^2 (EPIC-MOS) and 1227 cm^2 (EPIC-pn) at 1 keV.

- Two identical Reflection Grating Spectrometers (RGS) for high-resolution X-ray spectroscopy and spectro-photometry. The RGS are characterised by a bandpass of $0.35 - 2.5$ keV, a FOV $\sim 5'$, a timing resolution of 0.6 s, a spectral resolution of 0.04/0.025 Å and an effective area of 185 cm^2 at 1 keV.

- A 30 cm Optical Monitor (OM) telescope for optical/UV imaging and spectroscopy. The OM is characterised by a bandpass of $1800 - 6000$ Å, a FOV $\sim 17'$, a timing resolution of 0.5 s and a spatial resolution $\sim 1''$.

The three EPIC cameras and the two detectors of the RGS spectrometers reside in the focal planes of the X-ray telescopes, while the OM has its own telescope. The basic characteristics of *XMM-Newton* are:

- Simultaneous operation of all scientific instruments.

- A sensitivity of $\sim$ 1550 cm^2 at 1.5 keV for each of the three telescopes it carries.

- An angular resolution $\sim 6''$ for each X-ray telescope.

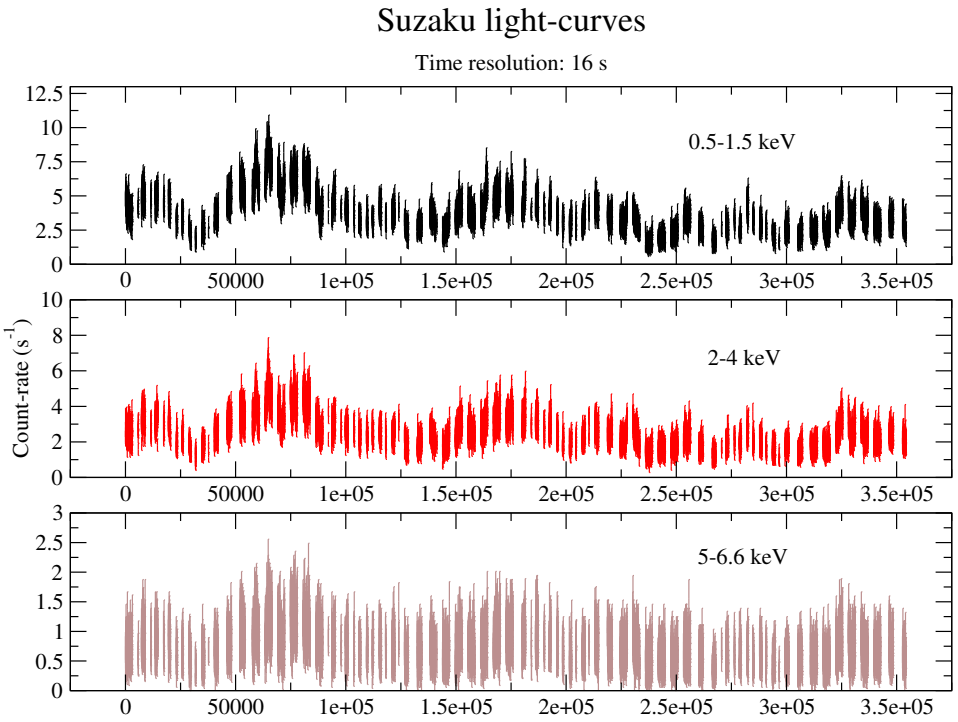

FIGURE 2.7: The final, combined XIS0, 2 and 3 light-curves for *Suzaku*'s Obs. 2 of MCG−6-30-15. Data points are represented by the centres of black (Soft band), red (Continuum band) and brown (Iron-line band) vertical lines whose width corresponds to twice the count-rate error. The time resolution is 16 s.

- Resolving power ($E/\Delta E \sim 20 - 50$) for the EPIC CCD cameras. This value is higher ($E/\Delta E \sim 200 - 800$) for the RGS spectrometers.
- Simultaneous optical/UV observations.
- Long and continuous target visibility for up to $\sim$ 40 h, which is especially favourable for studies of X-ray variability.

2.4.1 Observations of MCG−6-30-15 with XMM-Newton

MCG−6-30-15 has been observed five times by *XMM-Newton*; two times on July 2000 with on-source exposure times $\sim$ 43 and $\sim$ 55 ks and three times in 2001 (July and August) with significantly longer on-source exposure times ($\sim$ 83, 128 and 125 ks, respectively). More detailed information regarding the five observations are listed in Table 2.4. Columns 1, 2, 3 and 4 contain the observation number, *XMM-Newton* identification number of each observation, date at which each observation started (in a YYYY-MM-DD format) and total exposure time in units of ks, respectively.

TABLE 2.4: *XMM-Newton* observations of MCG−6-30-15.

Observation #	ID	Obs. date	Exp. time (ks)
Obs. 1	0111570101	2000-07-11	43.2
Obs. 2	0111570201	2000-07-11	55.0
Obs. 3	0029740101	2001-07-31	83.5
Obs. 4	0029740701	2001-08-02	127.5
Obs. 5	0029740801	2001-08-04	125.1

2.4.2 The final XMM-Newton light-curves

I acquired "background-subtracted" light-curves for a total of five *XMM-Newton* observations of MCG−6-30-15. An example of the "Soft", "Continuum" and "Iron-line" light-curves for Obs. 4 (which is the longest of the five observations) of MCG−6-30-15 with a temporal resolution of 1 ks is shown in Figure 2.8.

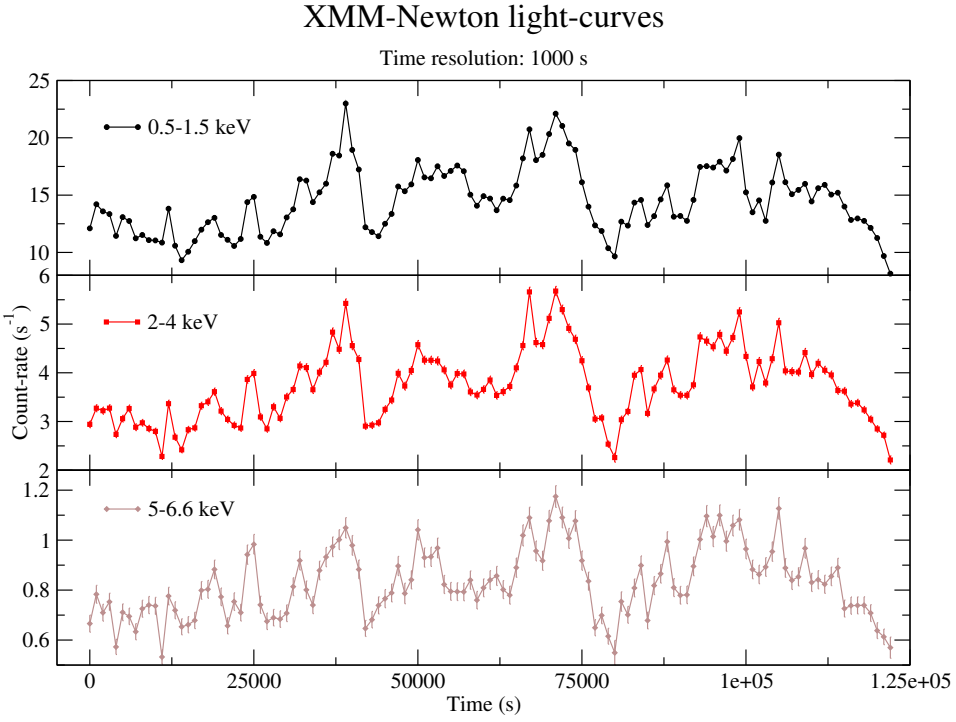

FIGURE 2.8: The "Soft" (black circles), "Continuum" (red squares) and "Iron-line" (brown diamonds) light-curves for *XMM-Newton*'s Obs. 4 of MCG−6-30-15. The time resolution is 1 ks, while an absence of error bars indicates their size is surpassed by the size of the data points. The lines joining the data points are put there purely to guide the eye.

Furthermore, a specific segment of the "Soft", "Continuum" and "Iron-line" light-curves for Obs. 4 is shown in Figure 2.9. The segment has a total length of 5 ks, while the time resolution is 10 s.

Comparing Figures 2.7 and 2.9 reveals the advantage of *XMM-Newton* over *Suzaku* − for a given segment the former offers continuous measurements, whereas the latter contains gaps. This is due to *XMM-Newton*'s highly eccentric orbit, which allows for continuous observation a certain target during a full orbit. Hence, even though *Suzaku* observations are typically longer than the corresponding *XMM-Newton* ones (see Figures

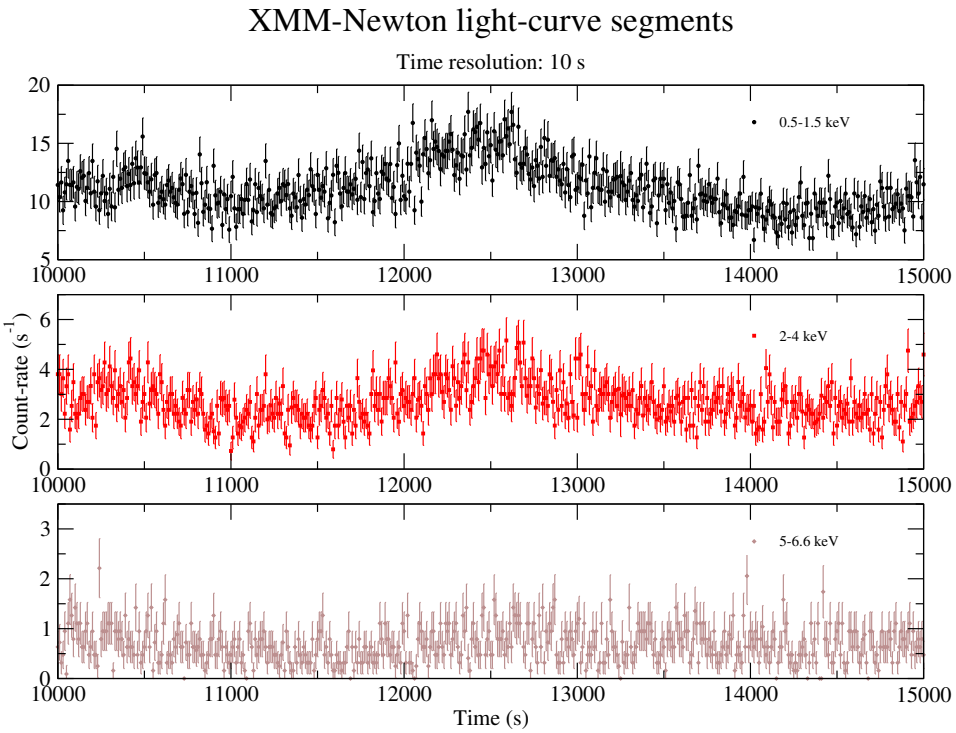

FIGURE 2.9: A 5 ks segment of the "Soft" (black circles), "Continuum" (red squares) and "Iron-line" (brown diamonds) light-curves for *XMM-Newton*'s Obs. 4 of MCG−6-30-15. The time resolution is 10 s.

2.1 and 2.4), the latter offers the ability to simultaneously probe long ($\sim$ 100 ks) as well as short ($\sim$ 100 s) time-scale variations.

Chapter 3

Time Series Analysis

3.1 Random processes

3.1.1 General overview

A physical process may, in general, be described mathematically by deterministic or stochastic functions, although in practice the majority of processes fall into the latter category and are appropriately referred to as *random (or stochastic) processes*. An observable $X(t)$ that arises from a physical process and depends on a certain parameter t (such as time) is called a *random process* if, for each t, the precise value for $X(t)$ cannot be determined theoretically, but has instead a range of possible values with an associated probability distribution describing the relative likeliness of each possible value.

Suppose that $X(t)$ arises from an experiment which may be repeated under identical conditions for a finite duration. During the first experiment, a record of $X(t)$ is obtained. Due to the random character of $X(t)$, any succession of experiments will, in general, yield a different record of $X(t)$ for the same duration. Hence, an observed record of a random process is merely one out of an *ensemble* of possible records, and each particular record is called a *realisation* of the process. For experiments that can be described by deterministic functions all realisations are identical.

In practice, the random character of most physical processes under study arise as a result of one or more of the following situations:

- The physical system generating the process may itself posses inherent random elements, such as the emission of photons from a celestial object.
- The system might be deterministic, but of such complex nature that it becomes impossible to describe its behaviour in any other way than in probabilistic terms.

- Even if the system is deterministic and sufficiently simple so that it can be described completely in terms of deterministic functions, the act of observing the system may cause contamination of the data by measurement errors. Therefore, the data must be regarded as random variables.

3.1.2 Time series analysis

The term *time series* is used to describe processes (either deterministic or random) that vary in time. *Time series analysis* refers to the body of principles and techniques that deal with the analysis of observed data from random processes in which the independent parameter t denotes time. In time series analysis the raw data usually take the form of a finite number of observations of a random process $X(t)$ for, say, $t = 1, 2, \ldots, N$ (in appropriate units). In effect, only a portion of a single realisation is given, and from these data one tries to infer as much information as possible about the properties of the whole process.

For the present work the available data are in the form of light-curves in three different energy bands, where the random variable $X(t)$ corresponds to the observed count-rate (or flux) of an X-ray source (MCG−6-30-15) and t is the time variable which takes the discrete values $t = \Delta t_{\rm bin}, 2\Delta t_{\rm bin}, \ldots, N\Delta t_{\rm bin}$, where $\Delta t_{\rm bin}$ is the time bin (for the *Suzaku* light-curves $\Delta t_{\rm bin} = 16$ s and 5760 s, while for the *XMM-Newton* light-curves $\Delta t_{\rm bin} = 10$ s). The purpose of my work is first of all to examine whether or not the light-curves between different energy bands are correlated, and secondly to determine the time-lag spectra between them.

3.2 Stationary random processes

3.2.1 General properties

In a variety of physical problems one encounters random processes which may be described loosely as being in a state of *statistical equilibrium*, i.e. for any realisation of such a process its statistical properties (such as the mean and variance) do not change over time. Random processes which posses this property are referred to as *stationary*. Stationary processes generally arise from "stable" systems that have achieved a "steady-state" mode of operation.

More precisely, if $\{X(t)\}$ is such a process, then since its statistical properties do not change with time, it follows that all possible values $X(t)$ must have the same probability density function. Furthermore, the property of stationarity implies that any doublet of the form $\{X(t_1), X(t_2)\}$ must have the same bivariate probability density function, every triplet of the form $\{X(t_1), X(t_2), X(t_3)\}$ must have the same trivariate probability density function, etc. This property can be summarised by stating that, for any set of time points $t_1, t_2, \ldots, t_n$, the joint probability distribution of $\{X(t_1), X(t_2), \ldots, X(t_n)\}$ must remain unaltered if each time point is shifted by the same amount. If this is true for any time shift, then the process $\{X(t)\}$ is said to be *completely stationary*.

Since complete stationarity is a rather restrictive requirement, it can be relaxed by introducing the notion of *stationarity up to order m*. Under this weaker condition one does not insist that the probability distribution of $X(t)$ must be identical to the probability distribution of $X(t+k)$ for all k, but merely their statistical their moments up to a certain order, say m. Hence, a process $\{X(t)\}$ is said to be stationary up to order m if, for any admissible sequence $t_1, t_2, \ldots, t_n$ and any k, all the joint moments up to order m of $\{X(t_1), X(t_2), \ldots, X(t_n)\}$ exist and are equal to the corresponding joint moments up to order m of $\{X(t_1+k), X(t_2+k), \ldots, X(t_n+k)\}$.

In the particular case of a stationary process up to order 2 (at least), the following properties can be shown to be satisfied (Priestley 1981; henceforth P81):

- The mean value $\text{Mean}\{X(t)\} \equiv \mu = E[X(t)]$ is a constant independent of time.
- The variance $\text{Var}\{X(t)\} \equiv \sigma^2 = E[(X(t)-\mu)^2]$ is a constant independent of time.
- The covariance $\text{Cov}\{X(t), X(s)\} \equiv E[\{X(t)-\mu\}\{X(s)-\mu\}]$ between any two points t, s is a function of the difference $(t-s)$ only.

Here E denotes the expectation operator. For example, assuming $X(t)$ is described by a continuous probability density function $f(x)$ (which, in the case of stationary time series, is expected not to have an explicit time-dependence), the mean of $X(t)$ is defined as the action of E on the variable $X(t)$, i.e.

$$\mu = E[X(t)] = \int_{-\infty}^{\infty} x f(x) \mathrm{d}x.$$

The variance and covariance are similarly defined by use of the definition of the expectation operator.

3.2.2 The auto-covariance function

In the case of time series there are several other properties one might be interested in, besides the mean and variance. One such property is the "memory" of the process, in the sense that one might wish to examine if a certain measurement $X(t)$ depends on how the system behaved in the past. Another question that arises is how long this "memory" is. One of the statistical functions that determines this "memory" is the *auto-covariance function (ACF)*, $R(\tau)$, which is defined as follows:

$$R(\tau) \equiv \text{Cov}\{X(t), X(t+\tau)\} = E[\{X(t)-\mu\}\{X(t+\tau)-\mu\}], \tag{1}$$

where τ is a real number and is usually called the "lag". For each value of τ, $R(\tau)$ measures the covariance between pairs of values of the process that are separated by an interval τ. As discussed in §3.2.1, the $R(\tau)$ is a function τ only. Furthermore, $R(\tau)$ possesses the following general properties (P81):

- $|R(\tau)| \leq R(0)$ for all τ.

- $R(-\tau) = R(\tau)$ for all τ, i.e. $R(\tau)$ is an even function of τ.

If the process $\{X(t)\}$ has no "memory", then the variables $X(t)$ and $X(t+\tau)$ must be independent. Hence $\mathrm{Cov}\{X(t), X(t+\tau)\} = 0$, implying that $R(\tau) = 0$. In addition, one might expect that $|R(\tau \to \infty)| \to 0$, meaning that the correlation between any two points of the process diminishes as their temporal separation increases (in effect, the process tends to "forget" what it did in the past).

3.2.3 The power spectral density

In the case of a deterministic function $X(t)$ that describes a stationary time series, Fourier analysis provides a powerful method for studying its "spectral" properties − i.e., if $X(t)$ is periodic it can be represented as a Fourier series, whereas if $X(t)$ in non-periodic (but decays sufficiently fast when $|t| \to \infty$), $X(t)$ can be represented as a Fourier integral. In the case of a stochastic stationary time series $X(t)$ there is no guarantee that a decomposition into sinusoids is feasible. Indeed, one would expect such a feat to be impossible, since $X(t)$ does *not* decay at infinity by virtue of its property of stationarity.

Nevertheless, progress can be made by means of a technique that depends on "truncating" a portion of a particular realisation of $X(t)$, which is considered to have zero mean (i.e. $\mu = 0$). In other words, one "chops off" the realisation at the points $t = \pm T$ for some arbitrary number T. By only considering the portion $X_T(t)$ of the realisation defined on the interval $-T \leq t \leq T$, one *can* assume that $X_T(t)$ may be expressed as a Fourier integral, i.e.

$$X_T(t) = \int_{-\infty}^{\infty} G_T(\omega) e^{\mathrm{i}\omega t} \mathrm{d}\omega, \tag{2}$$

$$G_T(\omega) = \frac{1}{2\pi} \int_{-T}^{T} X_T(t) e^{-\mathrm{i}\omega t} \mathrm{d}t, \tag{3}$$

where $G_T(\omega)$ is the Fourier coefficient of $X_T(t)$ at angular frequency ω.

If one considers the time-averaged value of $X_T^2(t)$ over the interval $[-T, T]$, then according to Parseval's identity (Tolstov 1976)

$$\frac{1}{2T} \int_{-T}^{T} X_T^2(t) \mathrm{d}t = \frac{1}{2T} \int_{-\infty}^{\infty} |G_T(\omega)|^2 \mathrm{d}\omega. \tag{4}$$

If the process $X(t)$ is assumed to be ergodic,[1] then the left-hand side of equation (4) corresponds to an estimate of the variance σ^2 of the process $X(t)$. Hence, one is lead to interpret $(|G_T(\omega)|^2/2T)\mathrm{d}\omega$ as being an estimate of the contribution to the total variance of the process $X(t)$ by sinusoidal components with frequencies between ω and $\omega + \mathrm{d}\omega$. Furthermore, since $X(t)$ is stationary, σ^2 is constant, and hence the limit of $(|G_T(\omega)|^2/2T)$ as $T \to \infty$ should exist. One therefore defines the *power spectral density (PSD)*,

[1] A process is called ergodic if time-averaged quantities are equal to their corresponding ensemble averages.

$h(\omega)$, of the process $X(t)$ as

$$h(\omega) = \lim_{T\to\infty} \left\{ E\left[\frac{|G_T(\omega)|^2}{2T} \right] \right\}, \tag{5}$$

where the ensemble average is considered in order to include all possible realisations of $X(t)$. One can show that there exists a particularly simple relation between $h(\omega)$ and $R(\tau)$, namely (P81)

$$R(\tau) = \int_{-\infty}^{\infty} h(\omega) e^{\mathrm{i}\omega\tau} \mathrm{d}\tau. \tag{6}$$

In other words, the PSD is the Fourier transform of the ACF. Since $R(0) = \sigma^2$, letting $\tau = 0$ in (6) gives $\sigma^2 = \int_{-\infty}^{\infty} h(\omega)\mathrm{d}\omega$. Hence, the integrated PSD is equal to the variance of the process.

3.2.4 Estimating the power spectral density in practice – the periodogram

Consider a source light-curve consisting of a set $\{X_r\}$ of N evenly sampled measurements of the source's flux $X(t)$ and a time bin Δt_{bin}, where $r = 1, 2, \ldots, N$. In practice more than one light-curves might be available, each of which is assumed to be evenly sampled with the same time bin Δt_{bin}, but with a varying N. One can then define the *discrete Fourier transform*, $\zeta_X(\omega)$, of each light-curve as

$$\zeta_X(\omega) = \sqrt{\frac{\Delta t_{\mathrm{bin}}}{N}} \sum_{r=1}^{N} X_r e^{-\mathrm{i}\omega t_r}, \tag{7}$$

where t_r takes the discrete values $\Delta t_{\mathrm{bin}}, 2\Delta t_{\mathrm{bin}}, \ldots, N\Delta t_{\mathrm{bin}}$ and ω takes any possible value. Once the DFT is known, one can then define the *periodogram*, $I(\omega)$, of each light-curve as follows:

$$I(\omega) = |\zeta_X(\omega)|^2. \tag{8}$$

As it turns out, the periodogram is a natural estimate of the PSD. In particular, it can be shown that the following properties are satisfied (P81):

- $E[I(\omega)] \to h(\omega)$, as $N \to \infty$.
- $\mathrm{Var}\{I(\omega)\} \to h^2(\omega)$, even as $N \to \infty$.
- For any fixed neighbouring angular frequencies ω_1 and ω_2, $\mathrm{Cov}\{I(\omega_1), I(\omega_2)\}$ decreases as N increases.
- The random variables $I(\omega)/2\pi h(\omega)$ are uncorrelated at the discrete set of frequencies $\omega_p = 2\pi p/N\Delta t_{\mathrm{bin}}$, where $p = 1, 2, \ldots, [N/2]$ (here $[N/2] = N/2$ if N is even and $[N/2] = (N+1)/2$ when N is odd).
- If $\{X_r\}$ are normally distributed, then the maximum likelihood estimate of $h(\omega_p)$ is $I(\omega_p)$.

The first property shows that the periodogram is an asymptotically unbiased estimate of the PSD. However, the second property means the periodogram is *not* a consistent estimate of the PSD. Furthermore, the

periodogram is expected to have an erratic and highly fluctuating form according to its third listed property. In practice, a technique that is often used for making the periodogram a consistent estimate of the PSD and reduce its fluctuating behaviour is the following:

1. Compute the periodogram of each source light-curve at the discrete set of frequencies ω_p.
2. Combine the periodogram estimates of each light-curve into a single periodogram sorted by increasing frequency.
3. Average neighbouring estimates of the combined periodogram.

According to the central limit theorem, the averaged periodogram estimates will thus tend to a Gaussian distribution with a mean value equal to the PSD.

3.3 Bivariate stationary processes

A *bivariate process* consists of two stochastic processes $\{X_1(t); X_2(t)\}$. A *stationary bivariate process* $\{X_1(t); X_2(t)\}$ is one whereby $\{X_1(t)\}$ and $\{X_2(t)\}$ are each stationary processes in the sense of §3.2. This is precisely the case of interest to the present work, since I wish to study possible correlations and time delays between two light-curves which are to be regarded as two random processes. In the following section I will present the statistical tools used to study correlations between bivariate stationary processes.

3.3.1 The cross-covariance and cross-correlation functions

Assuming the usual conditions of stationarity for $\{X_1(t)\}$ and $\{X_2(t)\}$, then one can define, in accordance with equation (1), the ACF of each process. The ACF describes correlation structures *within* a process. One can now introduce a new function, called the *cross-covariance function (CCF)*, which describes the correlation *between* two processes, and is defined as:

$$R_{12}(\tau) = \mathrm{Cov}\{X_2(t), X_1(t+\tau)\} = E[\{X_2(t) - \mu_2\}\{X_1(t+\tau) - \mu_1\}]. \tag{9}$$

The function $R_{12}(\tau)$ is to be thought as the cross-correlation function with "$X_1(t)$ leading $X_2(t)$". A crucial difference between the CCF and the ACF is that the former is not necessarily symmetric about the origin $\tau = 0$. For instance, suppose that $X_1(t) = X_2(t + \tau_0)$ for all t − i.e., the two processes are related by a constant time-lag τ_0. In that case, the CCF will be peaked at $\tau = \tau_0$.

3.3.2 The cross-spectrum

Defining the function $h_{12}(\omega)$, called the *cross-spectral density function* or, more briefly, the *cross-spectrumn (CS)*, as the Fourier transform of $R_{12}(\tau)$, one has

$$h_{12}(\omega) = \frac{1}{2\pi}\int_{-\infty}^{\infty} R_{12}(\tau)e^{-\mathrm{i}\omega\tau}\mathrm{d}\tau. \tag{10}$$

Of course, it is assumed that $h_{12}(\omega)$ exists for all ω. Clearly, CS provides the same information as CCF. However, in practice it is much more difficult to obtain an unbiased, consistent and independent estimate of the CCF. Furthermore, it is more difficult to interpret the information provided by the CCF, unless there is a simple relation between the two processes, such as a constant time-lag. On the other hand, the CS offers much more elucidating information that can be directly linked to physical processes, as will be shown shortly. I will therefore focus my attention on the theoretical aspects of the CS, as well as how one estimates this function in practice.

3.3.3 The phase spectrum and coherence function

Since $h_{12}(\omega)$ is, in general, a complex function (as $R_{12}(\tau)$ need not be symmetric about the origin), one may decompose it into its real and imaginary parts, i.e. $h_{12}(\omega) = \mathrm{Re}\{h_{12}(\omega)\} + \mathrm{iIm}\{h_{12}(\omega)\}$. An alternative way of expressing $h_{12}(\omega)$ is to write the function in "polar" form, i.e. $h_{12}(\omega) = |h_{12}(\omega)|e^{\mathrm{i}\phi_{12}(\omega)}$, where

$$\phi_{12}(\omega) = \arg\{h_{12}(\omega)\}. \tag{11}$$

The function $\phi_{12}(\omega)$ is called the *phase spectrum* and represents the average value of the phase shift, $\phi_1(\omega) - \phi_2(\omega)$, between the components in $X_1(t)$ and $X_2(t)$ at frequency ω. Since the phase spectrum is defined modulo 2π, it is customary to choose the principal value of $\phi_{12}(\omega)$ so that it is defined on the interval $(-\pi, \pi]$. By writing $\phi_{12}(\omega) = \omega\tau_{12}(\omega)$ one can thus introduce the so-called *time-lag spectrum*, $\tau_{12}(\omega)$, which represents the physical temporal delay between the components in $X_1(t)$ and $X_2(t)$ at frequency ω.

If the processes $X_1(t)$ and $X_2(t)$ are related by a linear transformation,[2] then the processes are said to be perfectly coherent in the sense that measuring $X_1(t)$ enables one to predict 100% of $X_2(t)$. A quantitative way to measure this degree of linear correlation is by means the so-called *coherence function*, which is defined as

$$\gamma_{12}^2(\omega) = \frac{|h_{12}(\omega)|^2}{h_1(\omega)h_2(\omega)}. \tag{12}$$

The coherence function may be interpreted as the degree of linear correlation, in the mean-squared sense, between the two processes (Nowak *et al.* 1999). As is the case with ordinary correlation coefficients,

[2] A linear transformation refers to either a simple linear relation of the form $X_1(t) = aX_2(t)$ where a is a constant, a costant time delay τ such that $X_1(t) = X_2(t+\tau)$ or a "smoothing" of the form $X_1(t) = \int_{-\infty}^{\infty} X_2(t-t')\Psi(t')\mathrm{d}t'$, where $\Psi(t)$ is the "smoothing" function which could also be interpreted as the "response" of $X_1(t)$ to $X_2(t)$. In all of these cases $\gamma_{12}^2(\omega) = 1$ for all ω.

$\gamma^2_{12}(\omega) \leq 1$ between any two processes. The case when $\gamma^2_{12}(\omega) \sim 1$ indicates a strong correlation, while $\gamma^2_{12}(\omega) \sim 0$ indicates a weak correlation. In the particular case when the two processes are uncorrelated, $R_{12}(\tau) = 0$ for all τ, hence $h_{12}(\omega) = 0$ for all ω and $\phi_{12}(\omega) = \gamma^2_{12}(\omega) = 0$ for all ω.

As a concrete example of a mechanism that results in the loss of coherence, suppose that the two processes satisfy a linear regression relationship of the form $X_1(t) = aX_2(t) + \varepsilon(t)$, where a is a constant and $\varepsilon(t)$ is a white noise (i.e. purely random) process, uncorrelated with $X_2(t)$. Such may be the case if the two processes represent two light-curves of the same source that are contaminated by counting (i.e. Poisson) noise. In that case, it can be shown that $\gamma^2_{12}(\omega) = [1 + \{h_\varepsilon(\omega)/a^2 h_2(\omega)\}]^{-1}$, where $h_\varepsilon(\omega)$ is the PSD of the noise process (P81). Hence, if $\varepsilon(t) = 0$ for all t, then the two processes are perfectly correlated and hence $\gamma^2_{12}(\omega) = 1$ for all ω. However, the presence of the noise component implies that $\gamma^2_{12}(\omega) < 1$ for all ω. Moreover, the coherence function goes to zero when the PSD of the noise becomes large. This implies that the two processes will appear to be completely uncorrelated when fluctuations due to counting noise dominate over the observed fluctuations of the two light-curves, even if the two processes are inherently perfectly coherent. Apart from the inevitable loss of coherence due to the presence of noise, the source that gives rise to the observed processes $X_1(t)$ and $X_2(t)$ might itself be inherently non-linear and thus lead to a loss of coherence.

Evidently, the phase spectrum and coherence function are of crucial importance in studying time delays and correlations between two light-curves at different frequencies (or time-scales), respectively. The final necessary step is to specify the "recipes" needed to estimate these functions from real data.

3.3.4 Estimating the phase spectrum and coherence function in practice

Consider a set $\{X_{1,r}, X_{2,r}\}$ of N uniformly sampled measurement pairs with a common time bin $\Delta t_{\rm bin}$, in the form of a pair of light-curves of a certain source that correspond to two different energy bands, where $r = 1, 2, \ldots, N$. In practice, there may be several such light-curve pairs available. The coherence function differs from the periodogram and time-lags in that it is only meaningful to talk of the coherence from an ensemble of independent measurements, which may be estimated by either considering separate light-curve pairs or consecutive frequencies (Vaughan & Nowak 1997; Nowak *et al.* 1999). The estimate of the coherence function, $\hat{\gamma}^2_{12}(\nu)$, at a frequency ν is computed by

$$\hat{\gamma}^2_{12}(\nu) = \frac{|\langle I_{12}(\nu)\rangle|}{\langle I_1(\nu)\rangle\langle I_2(\nu)\rangle} = \frac{\langle \zeta^*_{X_2}(\nu)\zeta_{X_1}(\nu)\rangle}{\langle |\zeta_{X_1}(\nu)|^2\rangle\langle |\zeta_{X_2}(\nu)|^2\rangle}, \tag{13}$$

where the angled brackets represent an averaging over consecutive frequency bins and/or light-curve pairs and $\zeta_{X_1}(\nu)$, $\zeta_{X_2}(\nu)$ are the usual DFTs of each light-curve for the two energy bands. In addition, $I_{12}(\nu)$ is called the *cross-periodogram* and is defined as

$$I_{12}(\nu) = \zeta^*_{X_2}(\nu)\zeta_{X_1}(\nu). \tag{14}$$

The periodograms as well as the cross-periodograms are computed following the steps outlined in §3.2.4. Assuming there are n measurements averaged in computing $\hat{\gamma}_{12}(\nu)$ at a particular frequency ν, then the 1σ uncertainty in $\hat{\gamma}^2_{12}(\nu)$, $\sigma_{\hat{\gamma}^2}(\nu)$, is (Vaughan & Nowak 1997)

$$\sigma_{\hat{\gamma}^2}(\nu) = \sqrt{\frac{2}{n}} \frac{\hat{\gamma}^2_{12}(\nu)[1 - \hat{\gamma}^2_{12}(\nu)]}{|\hat{\gamma}_{12}(\nu)|}. \tag{15}$$

In other words, $\sigma_{\hat{\gamma}^2}$ depends on the value of $\hat{\gamma}^2_{12}$ itself. In particular, the lower the estimated coherence (i.e. the less correlated the light-curves between the two energy bands are), the higher its error will be.

Having introduced the cross-spectrum, one can use equation (11) in order to introduce the natural estimate of the phase-lag, $\hat{\phi}_{12}(\nu)$, evaluated at a frequency ν:

$$\hat{\phi}_{12}(\nu) = \arg\{\langle I_{12}(\nu)\} \equiv \arctan\left[\frac{\langle \mathrm{Im}\{I_{12}(\nu)\}\rangle}{\langle \mathrm{Re}\{I_{12}(\nu)\}}\right]. \tag{16}$$

The corresponding 1σ error of $\hat{\phi}_{12}(\nu)$, $\sigma_{\hat{\phi}}(\nu)$, can be shown to equal (Nowak *et al.* 1999)

$$\sigma_{\hat{\phi}}(\nu) = n^{-1/2} \sqrt{\frac{1 - \hat{\gamma}^2_{12}(\nu)}{2\hat{\gamma}^2_{12}(\nu)}}. \tag{17}$$

The error in the time-lag is then simply $\sigma_{\hat{\phi}}/2\pi\nu$. According to (17), the lower the coherence between the two energy band light-curves for a given frequency, the larger the error in the estimate of the phase-lag (or time-lag). This behaviour may be understood from the fact that when $\gamma^2_{12}(\omega)$ is low, the phase spectrum is estimated by averaging the difference between the phases of two effectively independent complex-valued random variables ($\zeta_{X_1}(\omega)$ and $\zeta_{X_2}(\omega)$). In particular, when $\gamma^2_{12}(\omega) = 0$ for all ω, it may be shown that the principal value of $\hat{\phi}_{12}(\omega)$ is approximately uniformly distributed over the interval $(-\pi/2, \pi/2)$ (P81).

Chapter 4

Data Analysis and Results

In this chapter I describe how I used the *Suzaku* and *XMM-Newton* light-curves that I obtained following the procedures outlined in Chapter 2, in order to estimate the "Soft vs Continuum" and "Iron-line vs Continuum" time-lag spectra and coherence functions using the statistical tools developed in Chapter 3. I then discuss the effects and possible implications of combining the *Suzaku* and *XMM-Newton* light-curves, and attempt to interpret the estimated time-lag spectra within the context of the "illuminated disc" hypothesis.

4.1 The XMM-Newton data

The *XMM-Newton* data are composed of long and continuous light-curves binned at 10 s. The light-curve from Obs. 1 contain gaps of length > 200 s, thus I divided it into three segments. In addition to the time, count-rate and corresponding error, each point in the *XMM-Newton* light-curves is also characterised by a number referred to as the fractional exposure (FE), which corresponds to the total fraction of the time during which the satellite was recording data. The FE for the *XMM-Newton* light-curves is always below unity, with a typical value of ~ 0.7 due to the observational mode ("small window mode") with which the data were recorded. However, in some cases a point (or group of points) have a FE < 0.7. This is due to malfunctions of the satellite that result in the improper recording of data. In the case of *XMM-Newton*, I considered any point with FE < 0.35 as being a *missing point*. Figure 4.1 shows a particular ~ 12.5 ks long Soft band light-curve part from *XMM-Newton*'s Obs. 3 of MCG−6-30-15 (top panel), along with the corresponding FE (bottom panel). The lines joining the points in both panels are put there purely to guide the eye and make the identification of the missing points easier.

Since any estimates of the time-lag spectrum and coherence function are based on the study of continuously sampled light-curves (i.e. containing no missing points), it is important to know how many missing points each *XMM-Newton* light-curve contains. This is listed in Table 4.1, which contains the number of segments, their corresponding length and number of missing points within them for each observation.

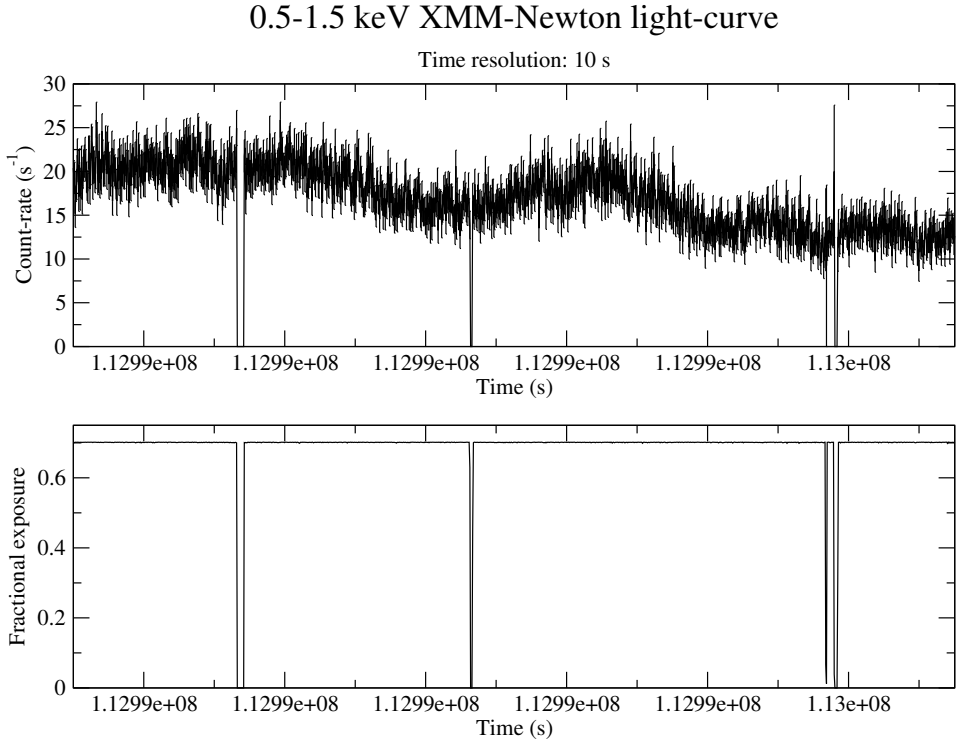

FIGURE 4.1: A particular $\sim$ 12.5 ks long Soft band light-curve from *XMM-Newton*'s Obs. 3 of MCG−6-30-15 (top panel), along with the corresponding FE (bottom panel). The lines joining the points in both panels are put there purely to guide the eye. The time resolution is 10 s.

TABLE 4.1: XMM-Newton 10 s-binned light-curves

	Obs. 1	Obs. 2	Obs. 3	Obs. 4	Obs. 5
Segments	3	1	1	1	1
Length (ks)	7.0, 1.0, 33.1	53	80.6	122.25	124.1
Mis. points	0, 0, 0	0	98	68	36

I thus performed a process of interpolation to "fill in" the missing points within the different light-curves as follows:

1. Count the number of missing data points in each light-curve.

2. If the above number is more than 10% of the total number of points in the segment, then do not include this segment in the subsequent analysis.

3. Identify if the missing points come in groups. If a particular group numbers ≤ 20 points (i.e. a width of ≤ 200 s), interpolate every point in the group. This threshold was chosen because the observed X-ray light-curves of MCG−6-30-15 have an amplitude smaller than the variations to the experimental Poisson noise at time-scales shorter than ~ 200 s.

4. Having identified a group of missing points that contains ≤ 20 points, search for the first point with FE > 0.35 right before and after the first and last point of the group. Find the straight line that

passes through those points and assume the missing ones lie on this line. In order to simulate the effect of random Poisson noise, add a value to the interpolated count-rate that corresponds to a Gaussian random number[1] with a mean of zero and a standard deviation equal to the average count-rate error of all non-zero measurements in the full light-curve.

An example of the result of the aforementioned interpolation procedure is shown in Figure 4.2, where a particular part of the "Soft" band light-curve of *XMM-Newton*'s Obs. 3 of MCG−6-30-15 is shown.

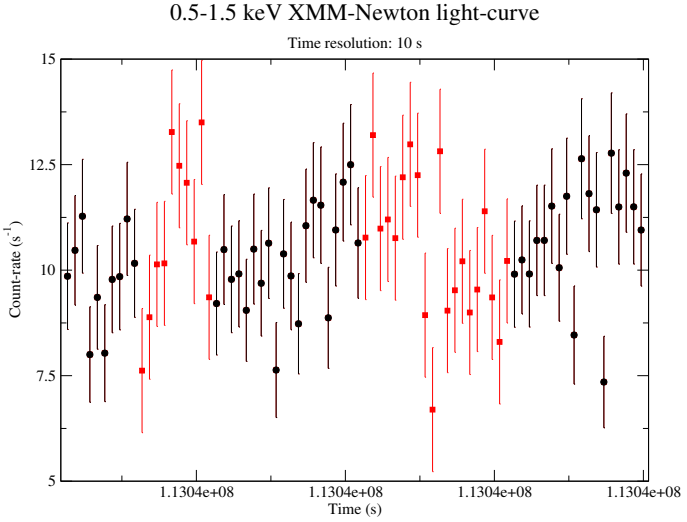

FIGURE 4.2: A particular 789 s long part of the "Soft" band light-curve from *XMM-Newton*'s Obs. 3 of MCG−6-30-15. The filled black circles correspond to measurements from the "raw" (i.e. uninterpolated) light-curve that contains two gaps, while the filled red squares correspond to data points that have been "filled in" using the interpolation scheme described in the text. The time resolution is 10 s.

Having interpolated all missing points in the *XMM-Newton* light-curves, I created new data files containing the "interpolated" light-curves that start at $t = 10$ s. Only "interpolated" light-curves that were longer than 10 ks (i.e. containing ≥ 1000 points) were considered in this work.

Estimating the phase spectra and coherence functions

There are a total of 5 such "interpolated" *XMM-Newton* light-curves (one for each observation), which I used in order to compute the "Soft", "Continuum" and "Iron-line" DFTs evaluated at the discrete frequencies ν_p by means of equation (7). The DFTs were then used to estimate the periodograms and cross-periodograms (real as well as imaginary parts) for the different energy bands using equations (8) and (14), thus obtaining a total of 20624 frequency estimates ($8.06 \times 10^{-6} - 5.00 \times 10^{-2}$ Hz) which I then sorted by increasing frequency. The first 67 of the sorted estimates ($8.06 \times 10^{-6} - 1.69 \times 10^{-4}$ Hz) were averaged to produce a single estimate (8.71×10^{-5} Hz), while the rest were averaged adopting a logarithmic binning scheme with a bin width of 1.4. These averaged estimates were then used to compute the time-lag spectra and coherence

[1] According to the Central Limit Theorem, the Poisson distribution tends to a Gaussian distribution when the number of events (or counts in the case of light-curves) becomes large.

functions between the different energy bands along with their corresponding errors according to equations (13), (15), (16) and (17).

The results are shown in Figure 4.3; in the top and bottom panels I plot the time-lag spectra and coherence functions for the "Soft vs Continuum" (filled black dots) and the "Iron-line vs Continuum" (filled red squares) bands respectively.

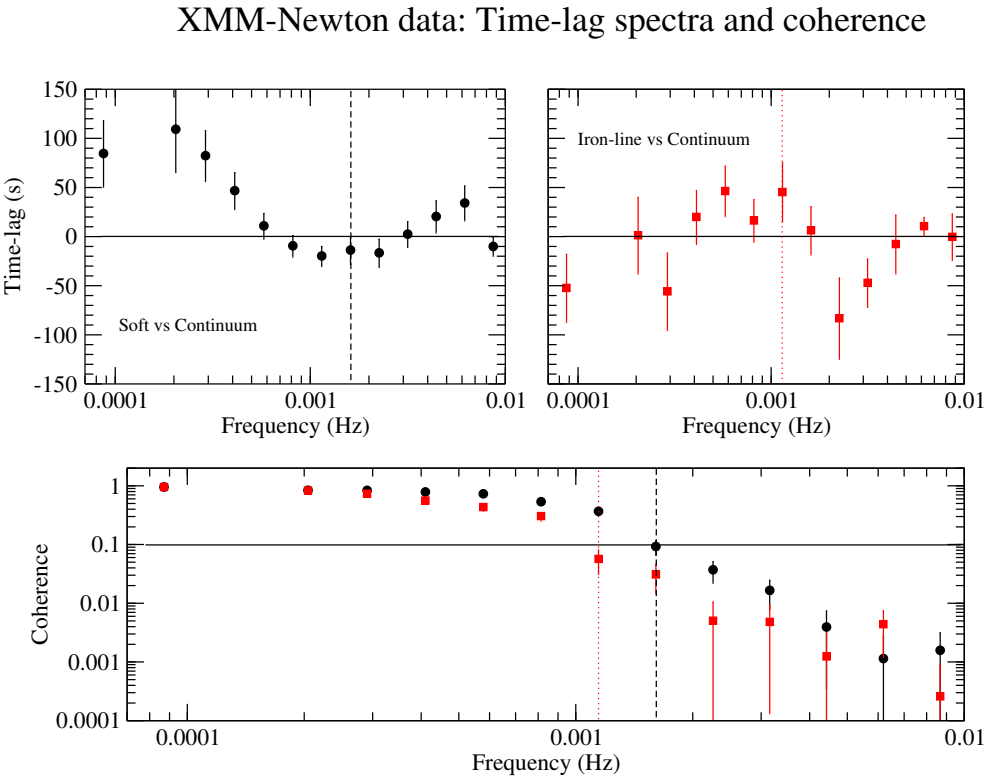

FIGURE 4.3: *Top panel*: The *XMM-Newton* time-lag spectrum for the "Soft vs Continuum" (filled black dots) and the "Iron-line vs Continuum" (filled red squares) bands. The horizontal line corresponds to a constant time-lag of zero. *Bottom panel*: The *XMM-Newton* coherence function for the "Soft vs Continuum" (filled black dots) and the "Iron-line vs Continuum" (filled red squares) bands.

The coherence function between the different energy bands is close to unity (i.e. perfect coherence) for the first ~ 2 points (i.e. $\lesssim 2 \times 10^{-4}$ Hz), and begins to drop at an approximately exponential rate at higher frequencies. The coherence between the "Iron-line" and "Continuum" bands drops even faster, which may be due to the lower S/N of the "Iron-line" band compared to the other energy bands. These results are consistent with the ones reported by Vaughan, Fabian & Nandra (2003), who also found a loss of coherence at frequencies $\sim 2 \times 10^{-4} - 10^{-3}$ Hz, albeit between different energy bands. Furthermore, the authors concluded that the loss of coherence at frequencies $\lesssim 10^{-3}$ Hz is intrinsic to the source and not an artifact of Poisson noise. As mentioned in Chapter 3, time-lag estimates that correspond to a low coherence are not reliable. I therefore adopted a coherence threshold of 0.1 above which any time-lag estimate will be considered as reliable. While the choice for this threshold is arbitrary, it is often adopted in practice. This can be made more rigorous with the use of simulations (e.g. Vaughan, Fabian & Nandra 2003). The 0.1

coherence threshold is indicated by black dashed and red dotted vertical lines in Figure 4.3 for the "Soft vs Continuum" and "Iron-line vs Continuum" estimates, respectively.

The "Soft vs Continuum" time-lag spectrum is observed to be "positive" and drops reciprocally with frequency $\lesssim 5 \times 10^{-4}$ Hz. At higher frequencies it becomes negative, attaining a minimum value of ~ -20 s at $\sim 10^{-3}$ s. It then appears to rise again towards positive values at $\sim 3 \times 10^{-3}$ Hz, although at these frequencies the coherence has already dropped significantly below 0.1, thus rendering any further conclusions questionable. The general shape of the "Soft vs Continuum" time-lag spectrum is consistent with the one reported by EMP11, although the estimated errors I obtained for the time-lag estimates are larger.

The "Iron-line vs Continuum" time-lag estimates have larger errors than the "Soft vs Continuum" ones, which may be due to the lower coherence between these two former energy bands. There seems to be a trend from negative to positive values in the range 8×10^{-5} Hz $- 10^{-3}$ Hz. Even though above $\sim 10^{-3}$ Hz the coherence is significantly below 0.1, the time-lag spectrum might again drop from positive to negative values.

4.2 The Suzaku data

The 16 s-binned *Suzaku* light-curves are in the form of a series of $\sim 1 - 3$ ks long segments separated by gaps of similar duration. The data points in the light-curves have FE = 1, except for the gaps between the segments. As discussed in Chapter 2, these gaps are due to the Earth being in the satellite's FOV, as well as the satellite passing through the SAA. Figure 4.4 shows a 30 ks-long part of the Soft band light-curve from *Suzaku*'s Obs. 2 of MCG−6-30-15 (top panel), along with the corresponding FE of each measurement (bottom panel).

Since any estimates of the time-lag spectrum and coherence function will be based on the study of those segments, it is important to know how many of them each *Suzaku* light-curve contains as well as their duration. Additionally, some segments are observed to contain points with FE = 0 (henceforth referred to as "missing points") which correspond to lack of observations due to malfunctions of the satellite. Table 4.3 lists the number of segments, their median and average length as well as the total number of missing points within all of them for each of the four observations.

Table 4.2: Suzaku 16 s-binned light-curves

	Obs. 1	Obs. 2	Obs. 3	Obs. 4
Segments	22	85	47	48
Med. length (s)	2336	1456	2144	1776
Av. length (s)	2129	1669	2081	1999
Mis. points	546	20	0	0

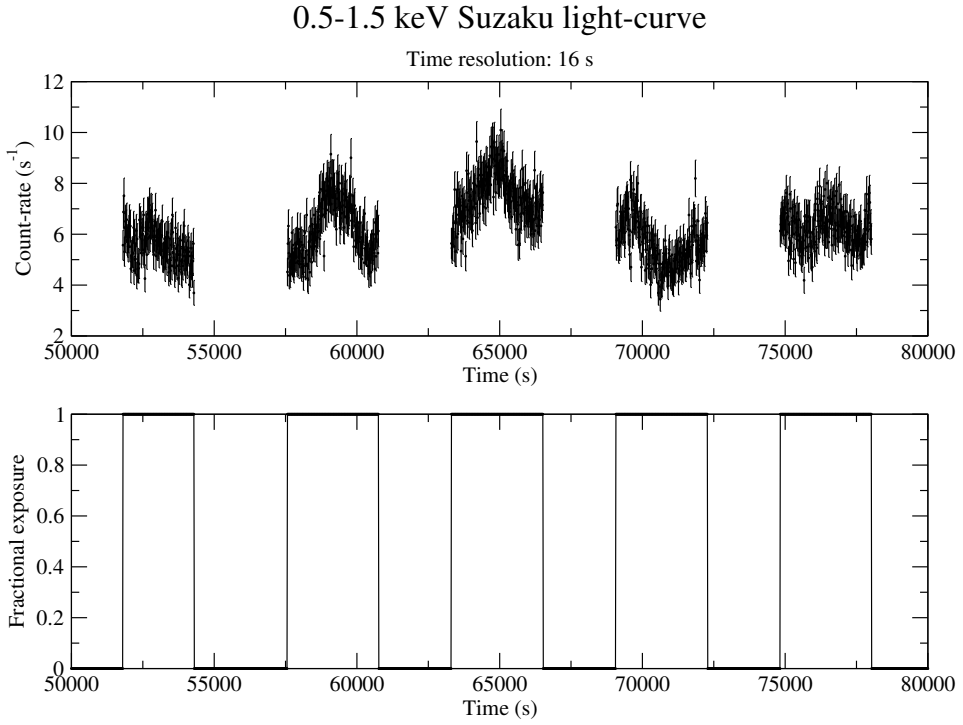

FIGURE 4.4: A particular part of the $0.5 - 1.5$ keV light-curve from *Suzaku*'s Obs. 2 of MCG−6-30-15 (top panel), along with the corresponding FE (bottom panel). The part contains five segments with a FE = 1, while the gaps have a FE = 0. The time resolution is 16 s.

The length of the segments is more or less symmetrically distributed about the average value. Furthermore, the number of missing points constitutes a negligible fraction of the total number of points in the Obs. 2-4 light-curves, except for Obs. 1, which is also the shortest of the four *Suzaku* observations. In the case of Obs. 1, the missing points are overwhelmingly distributed over the last 17 segments.

As in the case of the *XMM-Newton* light-curves, I performed the same process of interpolation discussed in §4.1 to "fill in" the missing points within the *Suzaku* light-curve segments. Those "interpolated" segments were then saved in separate data files. Only "interpolated" segments that were longer than 1600 s were considered in this work (i.e. containing ≥ 100 points). I thus obtained a total of 101, 16 s-binned *Suzaku* segments for each energy band.

Even though the minimum frequency that can be probed with the 16 s-binned *Suzaku* light-curve segments is $\sim 3 \times 10^{-4}$ Hz, one can use the full light-curves with a larger sampling period in order to probe even lower frequencies ($\sim 10^{-6}$ Hz). To this end, I binned the full *Suzaku* light-curves at 5760 s (which corresponds to *Suzaku*'s orbital period). The 5760 s-binned light-curves contain no gaps or missing points (see Figure 2.2). The total number of points in the full light-curves of each *Suzaku* observation as well as their corresponding length are listed in Table 4.4.

Since there are large number of missing points in the 16 s-binned Obs. 1 segments that are distributed over the last 17 segments (see Table 4.2), I did not include the 5760-s binned Obs. 1 light-curves in the subsequent analysis. I thus obtained a total of 3, 5760 s-binned *Suzaku* light-curves for each energy band.

TABLE 4.3: Suzaku 5760 s-binned light-curves

	Obs. 1	Obs. 2	Obs. 3	Obs. 4
Tot. points	15	62	38	37
Length (ks)	86.4	357.12	218.88	213.12

Estimating the time-lag and coherence spectra

For both the 16 and 5760 s-binned *Suzaku* segments and light-curves, I computed the "Soft", "Continuum" and "Iron-line" DFTs evaluated at the discrete frequencies ν_p by means of equation (7). The DFTs were then used to compute the periodograms and cross-periodograms for the different energy bands.

For the 16 s-binned segments I obtained a total of 2894 frequency estimates ($\sim 2.7 \times 10^{-4} - 3.2 \times 10^{-2}$ Hz) of the periodograms and cross-periodograms, which I then sorted by increasing frequency. I averaged the combined estimates adopting a logarithmic binning scheme with a bin size of 1.4 and computed the coherence and phase-lag along with their errors of the averaged estimates according to equations (13), (15), (16) and (17).

The 5760 s-binned light-curves yielded a total of 68 frequency estimates ($2.8 \times 10^{-6} - 8.9 \times 10^{-5}$ Hz), which I binned together at the average frequency value (4.5×10^{-5} Hz) to obtain a single phase-lag and coherence estimate. The results are shown in Figure 4.5. In the top and bottom panels I plot the estimated time-lag spectra and coherence functions for the "Soft vs Continuum" and the "Iron-line vs Continuum" bands, respectively. The filled black dots (open black dot) and filled red squares (open red square) correspond to the 16 s-binned segment (5760 s-binned light-curve) estimates for the "Soft vs Continuum" and "Iron-line vs Continuum" bands, respectively.

The coherence function between the different energy bands is very close to unity (i.e. perfect coherence) for the first ~ 2 points (i.e. $\lesssim 3 \times 10^{-4}$ Hz). The loss of coherence is more prominent for the "Iron-line vs Continuum" bands. This may be due to the lower S/N of the "Iron-line" band light-curves. The shape of the coherence function is similar to the one obtained from the *XMM-Newton* data, i.e. the coherence between the different energy bands drops below 0.1 at frequencies $\gtrsim \times 10^{-3}$ Hz. The 0.1 coherence threshold is indicated by vertical black dashed and red dotted lines in Figure 4.5 for the "Soft vs Continuum" and "Iron-line vs Continuum" estimates, respectively.

The "Soft vs Continuum" time-lag spectrum exhibits the same general trend as the one observed from the *XMM-Newton* data, in that the time-lags are positive for frequencies $\lesssim 10^{-3}$ Hz. However, the *Suzaku* time-lags are not as negative at $\sim 1 - 2 \times 10^{-3}$ Hz as the *XMM-Newton* ones. The "Iron-line vs Continuum" time-lags have larger errors than the "Soft vs Continuum" ones, and show a similar trend from "negative" to "positive" in the range 4×10^{-5} Hz $- 10^{-3}$ Hz as the ones observed for the *XMM-Newton* time-lags.

At first glance, a comparison between Figures 4.3 and 4.5 reveals there are some differences between the *XMM-Newton* and *Suzaku* estimates of the "Soft vs Continuum" time-lag spectrum. For instance, the

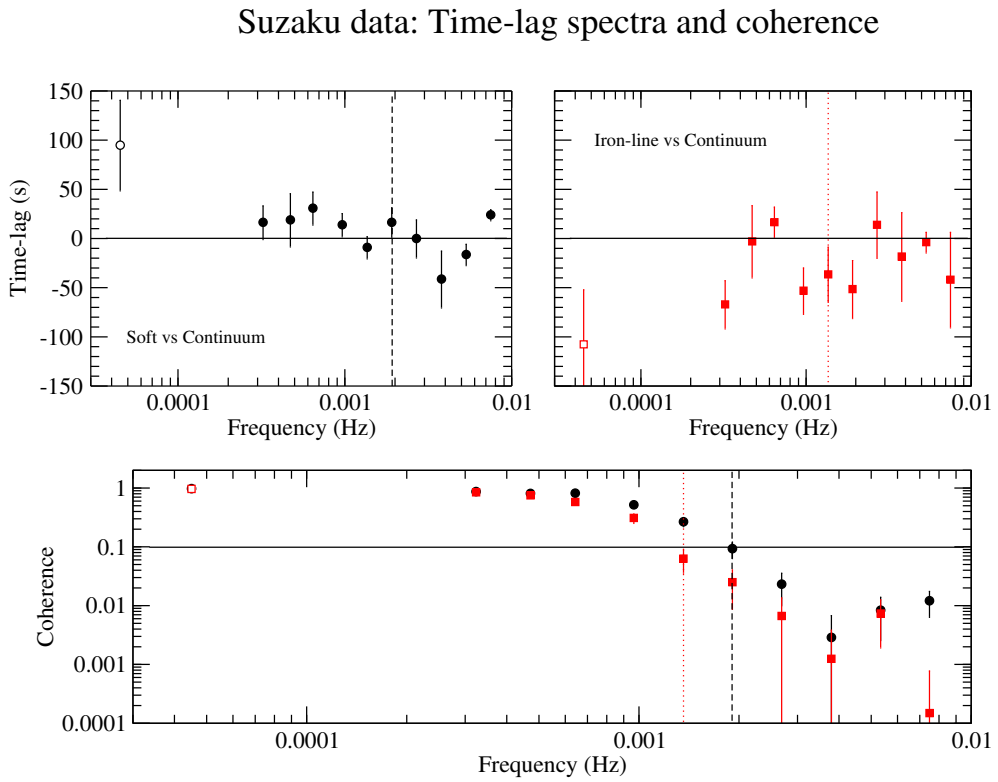

FIGURE 4.5: *Top panel*: The *Suzaku* time-lag spectrum for the "Soft vs Continuum" (filled and open black dots for the 16 s-binned segments and 5760 s-binned light-curves, respectively) and the "Iron-line vs Continuum" (filled and open red squares for the 16 s-binned and 5760 s-binned light-curves, respectively) bands. The horizontal line corresponds to a constant time-lag of zero. *Bottom panel*: The *Suzaku* coherence function for the "Soft vs Continuum" (filled and open black dots for the 16 s-binned segments and 5760 s-binned light-curves, respectively) and the "Iron-line vs Continuum" (filled and open red squares and diamonds for the 16 s-binned and 5760 s-binned light-curves, respectively) bands.

Suzaku estimates are mostly above the *XMM-Newton* ones in the frequency range $\sim 6\times10^{-4}-2\times10^{-3}$ Hz. At the same time, one might argue that the two independently estimated time-lag spectra agree within the errors of the estimates. The *XMM-Newton* and *Suzaku* "Iron-line vs Continuum" time-lag spectra also seem to be in agreement (within the errors), at least up to frequencies $\sim 7\times10^{-4}$ Hz. At higher frequencies the *Suzaku* estimates appear somewhat below the *XMM-Newton* ones, although by that time the coherence has already dropped below the 0.1 level for both estimates so no concrete conclusions can be drawn. In the following section I will assume that the *XMM-Newton* and *Suzaku* estimates can indeed be combined, and consider the properties of these combined estimates.

4.3 The combined time-lag spectra

The combined "Soft vs Continuum" and "Iron-line vs Continuum" time-lag spectra are shown in Figure 4.6, where the filled black dots and red squares correspond to *XMM-Newton* and *Suzaku* estimates, respectively.

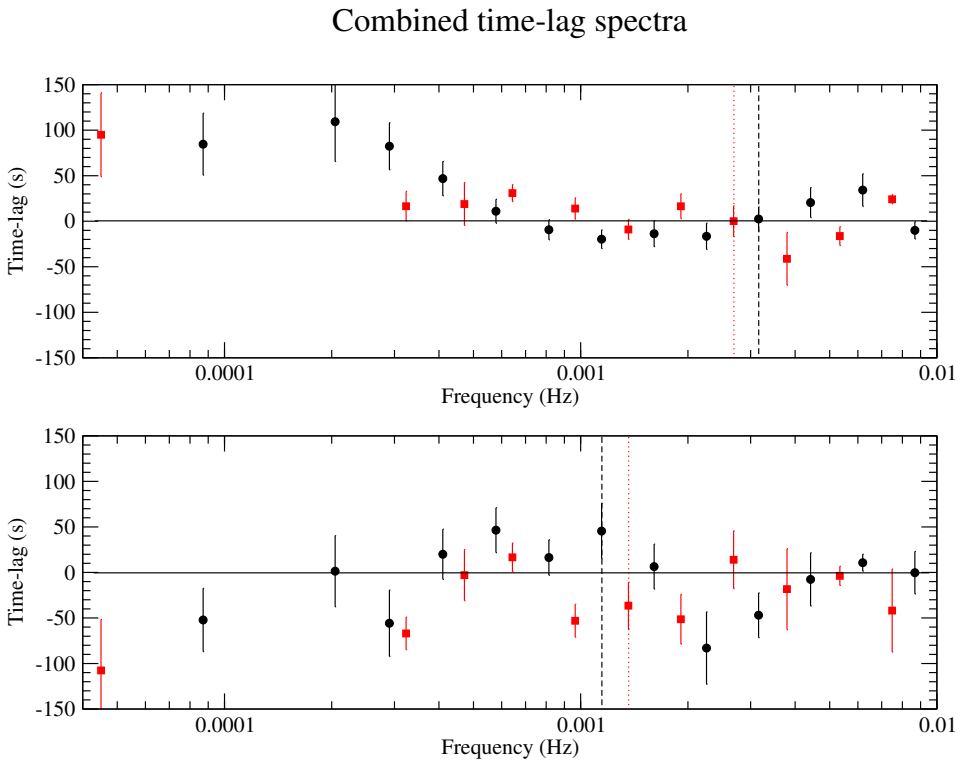

FIGURE 4.6: Combined time-lag spectra for the "Soft vs Continuum" (top panel) and "Iron-line vs Continuum" (bottom panel) bands. In both cases the filled black dots and red squares correspond to the *XMM-Newton* and *Suzaku* estimates, respectively. The continuous horizontal lines correspond to a constant time-lag of zero, while the vertical black dashed (*XMM-Newton*) and red dotted lines (*Suzaku*) correspond to coherence thresholds after which any time-lag estimates are considered as unreliable.

In the next section I develop a simple analytical model for the time-lag spectrum, within the context of the "illuminated disc" hypothesis. By fitting such a model to the estimated time-lag spectra, one may first of all investigate whether a simple "illuminated disc" scenario is consistent with my results. Furthermore, this procedure can also be used to ascertain whether the *XMM-Newton* and *Suzaku* time-lag estimates are consistent with each other, in that the parameters of a model that can adequately describe the *XMM-Newton* time-lag spectra should be consistent with the ones obtained by fitting the same model to the combined time-lag spectrum.

Before moving on to the next section, note that there is an agreement between the *XMM-Newton* and *Suzaku* "Soft vs Continuum" time-lag spectra in the range $\sim 1 - 3 \times 10^{-3}$ Hz. Hence, I decided to push the "limit of reliability" previously set to a coherence value of 0.1 and thereby extend the reliable *XMM-Newton* and *Suzaku* time-lag estimates by 2 and 1 points, respectively. These thresholds are indicated by vertical black dashed (*XMM-Newton* estimates) and dotted red (*Suzaku* estimates) lines in the top panel of Figure 4.6.

4.4 Modelling the estimated time-lag spectra

Let $X_1(t)$ and $X_2(t)$ denote the light-curves in the energy bands that represent the "Soft" and "Continuum" emission, respectively, of a certain source, of which only a particular realisation (represented by a sequence of discrete points) of finite duration is available each time.

In an "illuminated disc" scenario, the intrinsic time-lag spectrum can be determined theoretically by quantifying the "response" of the disc to the primary illuminating source. Let us assume that the observed "Soft" band light-curve is given by

$$X_1(t) = X_2(t) + \int_0^\infty \Psi(t')X_2(t-t')\mathrm{d}t', \tag{18}$$

where $\Psi(t)$ is the so-called *responce function* that describes the response of the "disc" to an instantaneous (i.e. delta-function) flash of "Continuum" emission. Given the linear relationship between the two processes given by (18), it may be shown that the CS between the two is (P81)

$$h_{12}(\omega) = h_2(\omega)[1 + 2\pi\tilde{\Psi}^*(\omega)], \tag{19}$$

where $\tilde{\Psi}(\omega)$ is the Fourier coefficient of the response function at frequency ω and is usually called the *transfer function*. Combining (11) and (19) for $\phi_{12}(\omega) = \omega\tau_{12}(\omega)$, one obtains the time-lag spectrum as a function of $\tilde{\Psi}(\omega)$:

$$\tau_{12}(\omega) = -\frac{1}{\omega}\arctan\left[\frac{2\pi\mathrm{Im}\{\tilde{\Psi}^*(\omega)\}}{1 + 2\pi\mathrm{Re}\{\tilde{\Psi}^*(\omega)\}}\right]. \tag{20}$$

Determining the time-lag spectrum thus boils down to determining the response function $\Psi(t)$.

An analytical approximation of the response function can be obtained by assuming a simple scenario whereby a point-source of "Continuum" emission is located at a constant height h above (along the axis of symmetry of the disc) and uniformly illuminating a disc of inner and outer radii $r_{\min}$ and $r_{\max}$, respectively (see Figure 4.8). If the reflector behaves as a "mirror" which is viewed from above and reflects a constant fraction f of the incident "Continuum" flux, then the response function can be approximated by

$$\Psi(t) = \begin{cases} f/\Delta t, & |t - t_0| \leq \Delta t/2 \\ 0, & |t - t_0| > \Delta t/2 \end{cases} \tag{21}$$

In other words, the response function is modelled as a "top-hat" function centered at t_0 with a width of Δt.[2] Qualitatively, one can understand the functional form of the response function given by (21) as follows:

[2] If the "Continuum" emission is assumed to be an instantaneous flash of light at $t = 0$ of the form $X_2(t) = \mathscr{E}\delta(t)$, where $\mathscr{E}$ is the total observed energy per unit area and $\delta(t)$ is the Dirac delta-function, then energy conservation dictates $\int_{t_0-(\Delta t/2)}^{t_0+(\Delta t/2)} X_2(t-t')\Psi(t')\mathrm{d}t' = f\mathscr{E}$. This suggests the functional form of the response function during the interval $|t-t_0| \leq \Delta t/2$ given by (21).

- The primary source emits a flash of light at $t = 0$ that reaches the disc at $t = t_0 - (\Delta t/2)$. Thus, during the interval $0 \leq t < t_0 - (\Delta t/2)$ the response function is identically zero since no "Soft" emission is observed.

- As an increasing number of photons from the flash reach further and further parts of the reflector's surface, the reflected emission remains constant (since, by assumption, the observer views the disc face-on) during the interval $t_0 - (\Delta t/2) \leq t \leq t_0 + (\Delta t/2)$.

- The reflected emission ceases when the last photons from the flash reach the outer parts of the reflector at $t = t_0 - (\Delta t/2)$. Hence the response function becomes identically zero again for $t > t_0 - (\Delta t/2)$.

The parameters are t_0 and Δt are clearly related to $r_{\rm min}$, $r_{\rm max}$ and h. Computing the Fourier transform of (21) one obtains the time-lag spectrum by means of (20):

$$\tau_{12}(\omega) = -\frac{1}{\omega} \arctan \left[\frac{f \mathrm{sinc}(\omega \Delta t/2) \sin \omega t_0}{1 + f \mathrm{sinc}(\omega \Delta t/2) \cos \omega t_0} \right], \tag{22}$$

where sinc denotes the sinc function.[3] As expected, when $f = 0$ there is no reflected emission and thus $\tau(\omega) = 0$ for all ω (i.e. the "Soft" and "Continuum" band light-curves coincide). The model described above is evidently highly approximate and simplistic in its conception, since it does not include important factors such as the inclination angle and possible GR effects that are bound to play an important role if the X-ray source and/or the disc are close to the SMBH. In addition, the disc should not realistically react as a perfect "mirror".

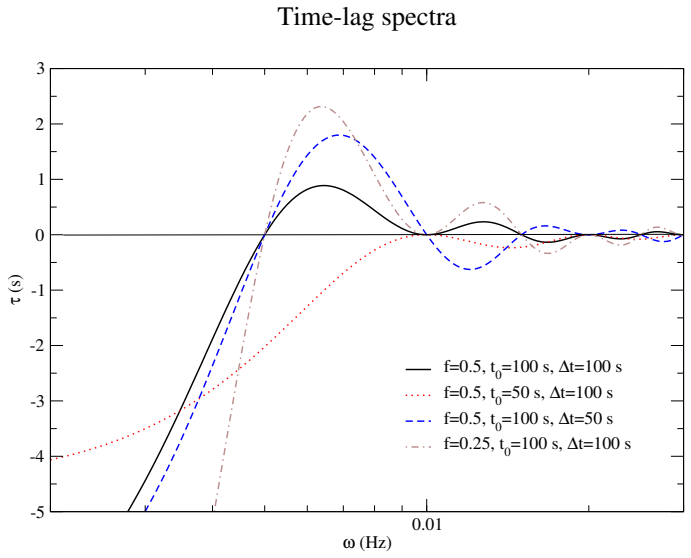

FIGURE 4.7: Time-lag spectra arising from a simple reflection scenario. The different coloured curves correspond to computed time-lag spectra for different parameter values f, t_0 and Δt of the analytic function given by equation (22).

[3] The function $\mathrm{sinc}(x)$ is defined as $\sin(x)/x$ for all $x \neq 0$.

To get a qualitative understanding of the behaviour of (22), Figure 4.7 shows different computed time-lag spectra for various values of the parameters f, t_0 and Δt. In general, the time-lags are, as expected, predominantly negative. As ω increases, $\tau_{12}(\omega)$ rises, reaches a maximum, and subsequently decays to zero (as dictated by (22) in the high-frequency limit) in an oscillatory fashion. Thus even in a simple reflection scenario such as the one considered above the time-lag spectrum can exhibit a complicated structure.

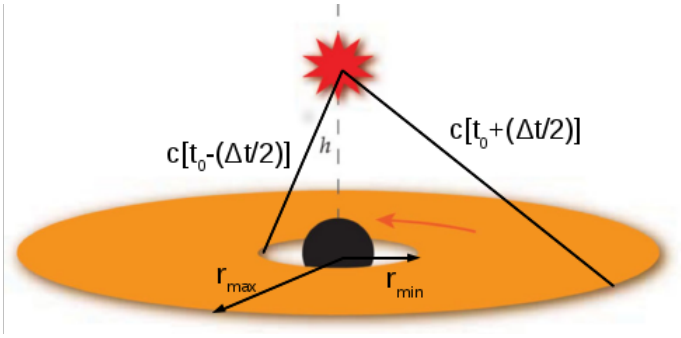

FIGURE 4.8: The geometry of an isotropic point source located at a height h on the rotation axis of an accretion disc with inner and outer radii $r_{\rm min}$ and $r_{\rm max}$, respectively. Original figure from Wilkins & Fabian (2012).

Clearly, the *XMM-Newton* and *Suzaku* estimates of the "Soft vs Continuum" time-lag spectrum are not consistent with a "reflection scenario" at low frequencies ($\lesssim 6 \times 10^{-4}$ Hz). EMP11 assumed a "power-law" function to fit the "positive" time-lags at low frequencies in MCG−6-30-15. Following their approach, I assumed the *XMM-Newton* time-lag spectrum can be modelled by a "power-law+top-hat" function of the form:

$$\tau_{12}(\nu) = C \left(\frac{\nu}{3 \times 10^{-4}\ \text{Hz}} \right)^{q} - \frac{1}{2\pi\nu} \arctan \left[\frac{f \text{sinc}(\pi\nu\Delta t) \sin(2\pi\nu t_0)}{1 + f \text{sinc}(\pi\nu\Delta t) \cos(2\pi\nu t_0)} \right], \tag{23}$$

where C and q are the normalisation and index of the "power-law" function that is assumed to model the "positive" time-lags. I did this in order to compare my results to the ones reported in the literature on the same object.

Fitting the "Soft vs Continuum" time-lags

I proceeded to fit the model function (23) to the *XMM-Newton* "Soft vs Continuum" time-lag spectrum in the frequency range $2 \times 10^{-4} - 3.2 \times 10^{-3}$ Hz (9 points in total; see Figure 4.6). The fitting was performed using the "Mathematica" command "NonlinearModelFit", which determines the best-fit parameters using a numerical χ^2 minimisation procedure. The results of the fit are listed in Table 4.4. The fit has a low value of $\chi^2_{\rm red}$ (0.24), indicating that the errors of the time-lags may be too conservative. However, the best-fit parameters of the model are in agreement (within the errors) with the ones reported by EMP11. The best-fit "power-law+top-hat" function is plotted as a continuous black curve in the top panel of Figure 4.9.

I then considered all the combined *XMM-Newton* and *Suzaku* time-lag spectrum at frequencies below 3.2×10^{-3} Hz (17 points in total; see Figure 4.6). When attempting to fit the "power-law+top-hat" function

to the combined time-lag spectrum, the resulting best-fit parameters are unconstrained and exhibit non-physical values with large errors. This result already suggests that the *XMM-Newton* and *Suzaku* time-lag spectra may not be consistent with each other after all. Nevertheless, I decided to "freeze" the values of f and t_0 to the ones obtained by fitting the *XMM-Newton* time-lags only, and repeated the fit in order to obtain more constrained values for the rest of the parameters. This approach of course already assumes the two time-lag spectra are consistent. The results of the fit are listed in Table 4.4. Although the $\chi^2_{\rm red}$ of the fit is high (1.52), it is still statistically acceptable ($P_{\rm null} = 0.09$). The best-fit "power-law+top-hat" function is plotted as a red dashed curve in the top panel of Figure 4.9.

While the normalisation of the "power-law", as well as the parameters of the "top-hat" function, are consistent (within the errors) with the ones obtained by fitting the *XMM-Newton* data only, the index q is flatter: $q_{\rm XMM+Suzaku} - q_{\rm XMM} = 0.60 \pm 0.22$. This difference is significant at the $\sim 2.7\sigma$ level, indicating that there is a disagreement between the combined and *XMM-Newton* data. The reason for this disagreement is because of the inclusion of the two low-frequency ($< 10^{-4}$ Hz) time-lag estimates in the combined "Soft vs Continuum" time-lag spectrum (something which has not yet been considered in the literature), which are consistently below what one would expect by extrapolating the best-fit "power-law" obtained by fitting the *XMM-Newton* data only.

TABLE 4.4: Best-fit parameters of a "power-law+top-hat" function to the XMM-Newton and combined time-lag spectra

Data*	Points	C (s)	q	f	Δt (s)	t_0 (s)	$\chi^2_{\rm red}$ ($P_{\rm null}$)
S vs C (X)	9	126.5 ± 14.6	-0.99 ± 0.20	0.83 ± 0.33	245 ± 7	122 ± 15	0.24 (0.96)
S vs C (X+Su)	18	91.5 ± 7.4	-0.39 ± 0.08	0.83	123 ± 78	122	1.52 (0.09)
I vs C (X+Su)	13	0	0	0.83	2337 ± 265	173 ± 60	1.92 (0.02)

* Su=*Suzaku*; XMM=*XMM-Newton*; S="Soft"; C="Continuum"; I="Iron-line"

Fitting the "Iron-line vs Continuum" time-lags

One of the most important parts of the present work is that time-lags have been estimated, for the first time, between the "Iron-line" and "Continuum" energy bands. So far, the "Soft" band has been used in the literature in order to represent the "reprocessing" effect of an illuminated disc. However, as remarked in Chapter 1, there are ambiguities as to the origin of the "Soft" band emission. The "Iron-line" band, however, if intrinsically broad, should represent a clear signal of reprocessing close to a SMBH, hence the study of its correlation with the "Continuum" band is ideal in testing the "illuminated disc" hypothesis.

Before attempting to fit the time-lags to a "power-law+top-hat" function, I first checked whether they are consistent with zero by fitting them to a constant time-lag τ_0, as one might suspect due to their large errors. The resulting fit yielded $\tau_0 = -(13 \pm 12)$ s, with a $\chi^2_{\rm red} = 3.11$, which is an unacceptable fit ($P_{\rm null} \sim 10^{-4}$). I thus proceeded to fit all the combined *XMM-Newton* and *Suzaku* (13 points in total) time-lags to a "power-law+top-hat" function.

When all the parameters of the model function were left as free, the fit yielded best-fit parameters with unconstrained and non-physical values with large errors. This might be due to the larger errors of the time-lag estimates compared to the "Soft vs Continuum" ones. Furthermore, the normalisation of the "power-law" function was found to be consistent with zero, thus I set $C = 0$. This is not necessarily surprising, since time-lags expected from a "power-law" function between the "Iron-line" and "Continuum" bands might be inherently smaller than the ones between the "Soft" and "Continuum" bands. In order to further constrain the parameters I assumed that $f = 0.83$, as obtained by fitting the *XMM-Newton* "Soft vs Continuum" time-lag spectrum. The results of the fit are listed in Table 4.4. The best-fit function is plotted as a black continuous curve in the bottom panel of Figure 4.9.

Although the parameter t_0 of the "top-hat" function is consistent with the one obtained by fitting both the *XMM-Newton* as well as the combined "Soft vs Continuum" time-lag spectrum, Δt is found to be entirely different. More importantly, the value of Δt I obtained is completely non-physical, since a result which indicates that $t_0 - (\Delta t/2) < 0$ implies the "response" of the disc to a flash "Continuum" emission occurs before the flash itself. Finally, in the bottom panel of Figure 4.9 I plot the best-fit "top-hat" function obtained by fitting the *XMM-Newton* "Soft vs Continuum" time-lags only as a red dashed curve. This curve is clearly morphologically inconsistent with the "Iron-line vs Continuum" time-lag spectrum.

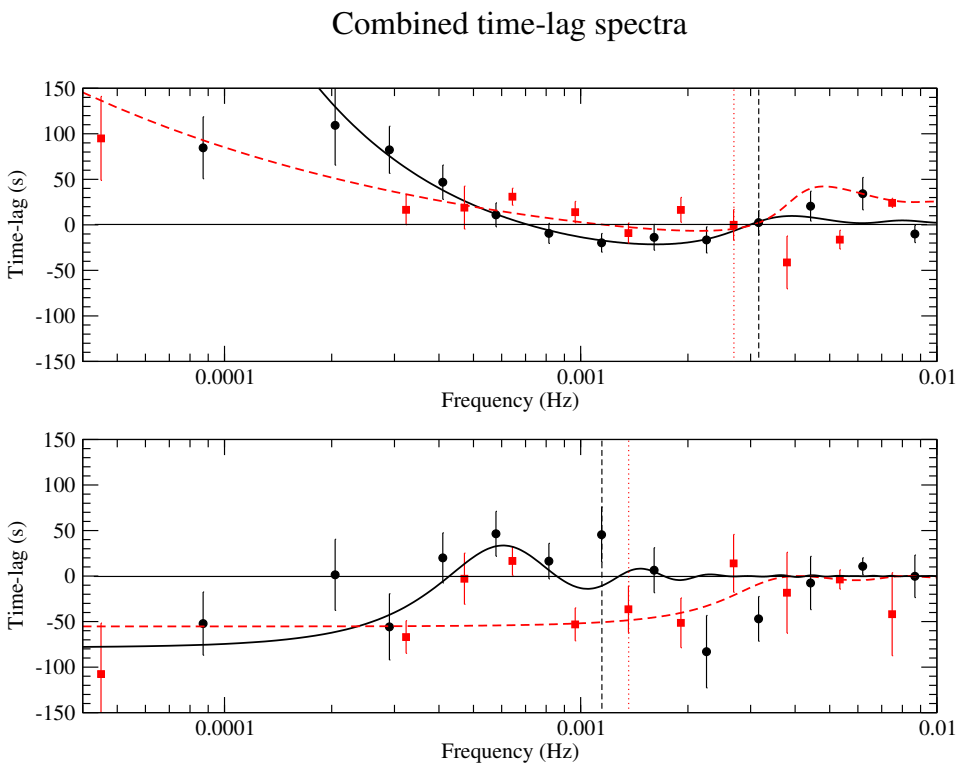

FIGURE 4.9: Combined "Soft vs Continuum" and "Iron-line vs Continuum" time-lag spectra, as in Figure 4.6. The continuous black and red dashed curves in the top panel correspond to best-fit "power-law+top-hat" functions obtained by fitting the *XMM-Newton* only and combined time-lags, respectively. The black continuous ad dashed red curves in the bottom panel correspond to best-fit "top-hat" functions obtained by fitting the combined and *XMM-Newton* only data, respectively.

Chapter 5

Summary and Concluding Remarks

At its core, this work is an attempt to understand the geometry of the inner-most region in AGN. This understanding is still incomplete and considerable effort is being made for the purpose of its advancement. X-ray variability studies strongly suggest that the X-ray source is located close to the central region in AGN, where a SMBH most probably resides. If this SMBH is surrounded and fuelled by material in the form of an accretion disc, then the X-ray source should illuminate the disc. This "illuminated disc" scenario is supported by the observed Fe Kα emission lines in the X-ray spectra of several "Type 1" (i.e. unobscured) AGN, which is interpreted as a signature of reflected emission from an optically thick disc. The observed shapes of those lines are, in most cases, found to be broad and "skewed" towards longer wavelengths, which is indicative of material orbiting close to a BH. The study of the Fe Kα line is therefore of primary importance in testing the "illuminated disc" hypothesis.

However, spectroscopy alone has been found to be consistent with different interpretations regarding the origin of the Fe Kα emission. A promising avenue for distinguishing between the different interpretations is the study of X-ray variability and, in particular, the time-lag spectrum between light-curves in energy bands that are thought to be representative of "primary" X-ray source and reflected emission from the disc, respectively.

Past studies have so far restricted their attention to determining the time-lag spectrum between light-curves in the "Soft" and "Continuum" energy bands. There is a good reason for this choice, as the current X-ray observatories such as *XMM-Newton* and *Suzaku* are most sensitive at energies < 2 keV. The results so far suggested that a simple reflection scenario is adequate to describe the observed "Soft vs Continuum" time-lag spectra in several AGN (e.g. MCG$-$6-30-15, Mrk 766, 1H 0707-495). In this work, I tried to "improve" these studies by considering *Suzaku* light-curves, in addition to *XMM-Newton* ones that have so far been used in the literature, in order to constrain the "Soft vs Continuum" time-lag spectrum.

However, and perhaps more importantly, since the origin of the "Soft" band emission still remains ambiguous, I attempted to determine, for the first time, the time-lag spectrum between the "Iron-line" and "Continuum"

bands. The "Iron-line" band has so far been neglected due to the low sensitivity of current X-ray satellites in this energy band.

To this end, I decided to determine the "Iron-line vs Continuum" time-lag spectrum of MCG−6-30-15 because it is X-ray bright and has been observed with many X-ray satellites. I thus collected all available *XMM-Newton* and *Suzaku* data on this source and obtained light-curves in the "Soft", "Continuum" and "Iron-line" energy bands.

The main results of my work can be summarised as follows:

- The "Soft" and "Continuum" band light-curves are found to be highly correlated (with a coherence of near unity) for frequencies $\lesssim 10^{-4}$ Hz and become increasingly uncorrelated for higher frequencies (exponential drop in coherence), in accordance with previous studies.
- The "Iron-line" band light-curves are found to be correlated with the "Continuum" band light-curves, although the degree of correlation between them is slightly weaker than the one found between the "Soft" and "Continuum" band light-curves. This could be an effect of Poisson noise, since its effect in the "Iron-line" light-curves is more significant.
- The "Soft vs Continuum" time-lag spectrum is found to be adequately described by a "power-law+top-hat" model whose parameters are consistent with past works if only the *XMM-Newton* time-lags are considered at frequencies $> 2 \times 10^{-4}$ Hz. Interestingly, this is also the frequency range where the coherence is found to start decreasing, which may be intrinsic to the source, so the time-lag estimation is more problematic. When the *Suzaku* data are included and all time-lag estimates at frequencies $< 2 \times 10^{-4}$ Hz are considered as well, the "power-law" flattens significantly. Although the rest of the parameters remain consistent (within the errors) with the ones obtained by fitting the *XMM-Newton* time-lags only, the error of the free parameter of the "top-hat" function increases significantly.
- The "Iron-line vs Continuum" time-lag spectrum is found to be inconsistent with zero. This result suggests that there is a certain "structure" in it. The time-lags show a tendency to rise from "negative" to "positive" values. This structure was investigated by attempting to fit the time-lags to a "top-hat" model function envisaged in a simple "reflection scenario", although the results yielded non-physical values for the model parameters. Furthermore, the best-fit "top-hat" function obtained by fitting the *XMM-Newton* "Soft vs Continuum" time-lag spectrum is found to be morphologically inconsistent with the corresponding "Iron-line vs Continuum" spectrum.

The detection and interpretation of "negative" time-lags remains an open issue. In order to further investigate this problem, more work has to be done in the following areas:

- Determine whether the *Suzaku* light-curves can be used to derive reliable time-lag estimates. This can be done through the use of simulations.

- Assign confidence limits on the reliability of time-lag estimates that have a low coherence value.
- Assess whether MCG−6-30-15 is stationary between the different light-curves. This is clearly important since all the statistical tools presented in Chapter 3 require the source to be stationary.
- Determine the effect of Poisson noise on the coherence functions.
- If time-lags in AGN scale with the mass of their SMBH, then the time-lag spectra of several sources with SMBHs of similar masses could be combined to further constrain the "Soft vs Continuum" and "Iron-line vs Continuum" time-lag spectra.
- Use realistic response functions between the "Iron-line" and "Continuum" bands that incorporate effects such as light-bending and inclination which are neglected in the simplistic "top-hat" functions that have so far been used to model "negative" time-lags in the "Soft vs Continuum" time-lag spectra.

Bibliography

Antonucci, R., 1993, ARA&A, 31:473-521

Arévalo, P.; Papadakis, I. E.; Uttley, P.; McHardy, I. M.; Brinkmann, W., 2006, MNRAS, 372:401-409

Arévalo, P.; McHardy, I. M.; Summons, D. P., 2008, MNRAS, 388:211-218

Arnaud, K. A.; Branduardi-Raymont, G.; Culhane, J. L.; Fabian, A. C.; Hazard, C.; McGlynn, T. A.; Shafer, R. A.; Tennant, A. F.; Ward, M. J., 1985, MNRAS, 217:105-113

Arons, J.; Kulsrud, R. M.; Ostriker, J. P., 1975, ApJ, 198:687-707

Bianchi, S.; Guainazzi, M.; Matt, G.; Fonseca Bonilla, N.; Ponti, G., 2009, A&A, 495:421-430

Burbidge, G. R., 1961, Nature, 190:1053-1056

Cameron, A. G. W., 1962, Nature, 194:963-964

Chartas, G.; Kochanek, C. S.; Dai, X.; Poindexter, S.; Garmire, G., 2009, ApJ, 693:174-185

Chartas, G.; Kochanek, C. S.; Dai, X.; Moore, D.; Mosquera, A. M.; Blackburne, J. A., 2012, ApJ, 757:137-148

Crummy, J.; Fabian, A. C.; Gallo, L.; Ross, R. R., 2006, MNRAS, 365:1067-1081

Dai, X.; Kochanek, C. S.; Chartas, G.; Kozlowski, S.; Morgan, C. W.; Garmire, G.; Agol, E., 2010, ApJ, 709:278-285

Danese, L.; Franceschini, A.; de Zotti, G.; Fasano, G., 1986, A&A, 161:1-6

De Marco, B.; Ponti, G.; Cappi, M.; Dadina, M.; Uttley, P.; Cackett, E. M., Fabian, A. C.; Miniutti, G., 2013, MNRAS, 431:2441-2452

Done, C.; Davis, S. W.; Jin, C.; Blaes, O.; Ward, M., 2012, MNRAS, 420:1848-1860

Emmanoulopoulos, D.; McHardy, I. M.; Papadakis, I. E., 2011, MNRAS, 416:L94-L98

Fabian, A. C.; Rees, M. J., Stella, L.; White, N. E., 1989, MNRAS, 238:729-736

Fabian, A. C.; Vaughan, S.; Nandra, K.; Iwasawa, K.; Ballantyne, D. R.; Lee, J. C.; De Rosa, A.; Turner, A.; Young, A. J., 2002, MNRAS, 335:L1-L5

Fabian, A. C.; Zoghbi, A.; Ross, R. R.; Uttley, P.; Gallo, L. C.; Brandt, W. N.; Blustin, A. J.; Boller, T.; Caballero-Garcia, M. D.; Larsson, J.; Miller, J. M.; Miniutti, G.; Ponti, G.; Reis, R. C.; Reynolds, C. S.; Tanaka, Y.; Young, A. J., 2009, Nature, 459:540-542

George, I. M.; Fabian, A. C., 1991, MNRAS, 249:352-367

Gliozzi, M.; Papadakis, I. E.; Grupe, D.; Brinkmann, W. P.; Räth, C., 2013, MNRAS, 433:1709-1717

Haardt, F.; Maraschi, L., 1991, ApJ, 380:L51-L54

Haardt, F.; Maraschi, L.; Ghisellini, G., 1994, ApJ, 432:L95-L99

Ho, L. C.; Filippenko, A. V.; Sargent, W. L. W., 1997, ApJ, 487:568-578

Kotov, O.; Churazov, E.; Gilfanov, M., 2001, MNRAS, 327:799-807

Laor, A., 1991, ApJ, 376:90-94

Lynden-Bell, D., 1969 Nature, 223:690-694

Markowitz, A.; Papadakis, I.; Arévalo, P.; Turner, T. J.; Miller, L.; Reeves, J. N., 2007, ApJ, 656:116-128

McHardy, I. M., 1989, In *Proc. 23rd ESLAB Symp.*, ed. J. Hunt, B. Battrick, p. 1111, Paris: European Space Agency

McHardy, I. M.; Papadakis, I. E.; Uttley, P.; Page, M. J.; Mason, K. O., 2004, MNRAS, 348:783-801

McHardy, I. M.; Gunn, K. F.; Uttley, P.; Goad, M. R., 2005, MNRAS, 359:1469-1480

McHardy, I. M.; Arévalo, P.; Uttley, P.; Papadakis, I. E.; Summons, D. P.; Brinkmann, W.; Page, M. J., 2007, MNRAS, 382:985-994

Miller, L.; Turner, T. J.; Reeves, J. N., 2008, A&A, 483:437-452

Miniutti, G.; Fabian, A. C., 2004, MNRAS, 349:1435-1448

Miniutti, G.; Fabian, A. C.; Anabuki, N.; Crummy, J.; Fukazawa, Y.; Gallo, L.; Haba, Y.; Hayashida, K.; Holt, S.; Kunieda, H.; Larsson, J.; Markowitz, A.; Matsumoto, C.; Ohno, M.; Reeves, J. N.; Takahashi, T.; Tanaka, Y.; Terashima, Y.; Torii, K.; Ueda, Y.; Ushio, M.; Watanabe, S.; Yamauchi, M.; Yaqoob, T., 2007, PASJ, 59:315-325

Narayan, R.; Yi, I., 1994, ApJ, 428:L13-L16

Nayakshin, S.; Melia, F., 1997, ApJ, 490:L13-L16

Nowak, M. A.; Vaughan, B. A.; Wilms, J.; Dove, J. B.; Begelman, M. C., 1999, ApJ, 510:874-891

Papadakis, I. E.; Nanadra, K.; Kazanas, D., 2001, ApJ, 554:L133-L137

Pounds, K. A.; Nandra, K.; Stewart, G. C.; George, I. M.; Fabian, A. C., 1990, Nature, 344:132-133

Poutanen, J.; Fabian, A. C., 1999, MNRAS, 306:L31-L37

Press, W. H.; Flannery, B. P.; Teukolsky, S. A.; Vetterling, W. T., 1992, *Numerical Recipes in Fortran 77: The Art of Scientific Computing*, Cambridge University Press, Cambridge

Priestley, M. B., 1981, *Spectral Analysis and Time Series*, Academic Press Inc., London

Reig, P.; Kylafis, N. D.; Giannios, D., 2003, A&A, 403:L15-L18

Ross, R. R.; Fabian, A. C., 2005, MNRAS, 358:211-216

Salpeter, E. E., 1964, ApJ, 140:796-800

Shakura, N. I.; Sunyaev, R. A., 1973, A&A, 24:337-355

Shapiro, S. L.; Lightman, A. P.; Eardley, D. M., 1976, ApJ, 204:187-199

Spitzer, L. Jr.; Saslaw, W. C., 1966, ApJ, 143:400

Sriram, K.; Agrawal, V. K.; Rao, A. R., 2009, ApJ, 700:1042-1046

Sunyaev, R. A.; Titarchuk, L. G., 1980, A&A, 86:121-138

Tanaka, Y.; Nandra, K.; Fabian, A. C.; Inoue, H.; Otani, C.; Dotani, T.; Hayashida, K.; Iwasawa, K.; Kii, T.; Kunieda, H.; Makino, F.; Matsuoka, M., 1995, Nature, 375:659-661

Tennant, A. F.; Ward, M. J., 1985, MNRAS, 217:105-113

Tolstov, G. P., 1976, *Fourier Series*, Dover Publications Inc., New York

Vasudevan, R. V.; Fabian, A. C., MNRAS, 2007, 381:1235-1251

Vaughan, S.; Fabian, A. C.; Nandra, K., 2003, MNRAS, 339:1237-1255

Zel'dovich, Ya. B., 1964, Soviet Physics Doklady, 9:195

Zoghbi, A.; Fabian, A. C.; Uttley, P.; Miniutti, G.; Gallo, L. C.; Reynolds, C. S.; Miller, J. M.; Ponti, G., 2010, MNRAS, 401:2419-2432

Zoghbi, A.; Uttley, P.; Fabian, A. C., 2011, MNRAS, 412:59-64